Inoperability Assessment of Interdependent Critical Infrastructures exposed to Natural Hazards considering Climate Change

Maria Valentina Clavijo Mesa[a], Matteo Broggi[b], Francesco Di Maio[a,*], Enrico Zio[c,a]

[a]*Energy Department, Politecnico di Milano, Milan, Italy*
[b]*Institute for Risk and Reliability, Leibniz University Hannover, Hannover, Germany*
[c]*MINES Paris-PSL University, Centre de Recherche sur les Risques et les Crises (CRC), Sophia Antipolis, France*

Abstract

Critical Infrastructures (CIs) are interdependent and, thus, vulnerable to scenarios of cascading effects, e.g., initiated by natural hazardous events like flooding, windstorms, heat waves, etc, which can lead to partial or complete inoperability. Traditional approaches for CI inoperability assessment are based on historical data of natural event occurrence and deterministic climate projections, which often neglect spatial correlations, thus limiting the analysis to the footprint of the direct failures on the CI in the location of occurrence of the hazardous event. Additionally, for long-term CI projections lifespans, it is necessary to consider the changes in natural hazards frequency and intensity due to climate change. In this work, we use climate projections to generate spatially coherent natural hazard scenarios through Stochastic Fields (SFs) via Karhunen–Loève Expansion (KLE), so that spatial dependencies and correlations across the CIs are preserved also accounting for climate change on the long-term. The generated hazard scenarios are integrated within the Dynamic Inoperability Input-output Model (DIIM) framework to evaluate the cascading effects on multi-state interdependent CIs. The overall modeling methodology and simulation framework is applied to multi-state interdependent power and water networks positioned in the climate conditions of North of Italy, considering to climate change projections based on Representative Concentration Pathways (RCPs), specifically RCP 4.5 and RCP 8.5. The analysis performed allows considering how climate change alters inoperability patterns and how systemic risks propagate across CIs. This provides insights for the design of mitigation and prevention strategies.

Keywords: Critical Infrastructures, Interdependency, Cascading Effects, Inoperability Assessment, Natural Hazard, Climate Change, Stochastic Field, Dynamic Inoperability Input-output Model.

[*]Corresponding author at: Via Privata Giuseppe La Masa 34, 20156 Milano MI, Italy.
Email address: francesco.dimaio@polimi.it

Nomenclature

$\mathcal{H}$	Set of natural hazards
H^*	Selected natural hazard characteristic variable

$\mathcal{D}$	Geographical extent (spatial domain) of the system of systems
Δ_s	Spatial resolution
$\bar{d}$	Coordinates (longitude, latitude) of the spatial locations in $\mathcal{D}$
$\bar{d}_l$	Coordinates (longitude, latitude) of the l-th grid location
$\mathcal{T}$	Temporal domain of the historical data
$H^*(\bar{d},t)$	Hazard intensity of H^* at time t, evaluated at each $\bar{d}$
τ	Threshold value of H^*
$\mathcal{T}_E$	Set of time instants for which $H^*(\bar{d},t) > \tau$
$\mathcal{F}$	Set of candidate probability distributions
F_p	Candidate p-th distribution
$\theta^*_{l,p}$	Parameters of the p-th distribution, at the l-th grid location
$F_l(\cdot)$	Marginal cumulative distribution function for $H^*(\bar{d},t), t \in \mathcal{T}_E$ at the l-th grid location
$u_l(t)$	Transformed (uniform) hazard value at the l-th location at time t
$Z_l(t)$	Gaussian anamorphosis of $u_l(t)$
h_{lo}	Haversian distance between l-th and o-th grid locations
$\rho(\cdot)$	Parametric spatial correlation function
$\bar{\bar{C}}$	Spatial correlation matrix
k	Number of retained eigenmodes
ς	Variance-retention threshold value
S	Set of synthetic hazard scenarios
$\bar{h}^s$	Hazard field in the s-th scenario
u_l^s	Uniform hazard value at the l-th location in in the s-th scenario
h_l^s	Hazard intensity at the l-th location in in the s-th scenario
$h^s_{e_{op}^{(i,i)}}$	Maximum hazard intensity along edge $e_{op}^{(i,i)}$ in in the s-th scenario
$\mathbb{P}(x^i_{z,f} \mid h_l^s)$	Probability that node n_z^i is in state $x^i_{z,f}$ given h_l^s
μ, β	Fragility curve parameters (mean, dispersion)
$\Phi(\cdot)$	Standard normal cumulative distribution function
M	Number of interdependent critical infrastructures
G^i	Directed graph of the i-th critical infrastructure
N^i	Set of nodes in the i-th critical infrastructure
n_z^i	z-th node of the i-th critical infrastructure
$E^{(i,i)}$	Set of edges in the i-th critical infrastructure
$e_{op}^{(i,i)}$	Edge from node n_o^i to n_p^i in the i-th critical infrastructure
$E^{(\mathrm{i,j})}$	Set of edges from the i-th infrastructure to the j-th infrastructure
$\mathrm{x}^{\mathrm{i}}_{\mathrm{z,f}}$	f-th performance state of z-th node in the i-th critical infrastructure
$\mathrm{x}^{\mathrm{i}}_{\mathrm{e}^{(\mathrm{i,i})}_{\mathrm{op}},\mathrm{u}}$	u-th performance state of edge from node n_o^i to n_p^i in the i-th infrastructure
$\bar{q}(t)$	Inoperability vector of the M critical infrastructures at time t
$q_i(t)$	Inoperability value of the i-th critical infrastructure at time t
$\bar{c}(t)$	Perturbation vector at time t
$\bar{\bar{A}}(t)$	Multi-state interdependency matrix at time t
$a_{ij}(q_j(t-1))$	Interdependency coefficient from the j-th infrastructure to the i-th infrastructure, based on $q_j(t-1)$
$\bar{\bar{\bar{K}}}$	Recovery matrix
k_{ii}	Recovery rate of the i-th infrastructure
T_i	Time for the i-th critical infrastructure to recover from inoperability $q_i(0)$ to

$q_i(T_i)$	
r^j	Set of discrete inoperability intervals of the j-th critical infrastructure
r_w^j	w-th inoperability interval of the j-th critical infrastructure
$a_{ij}(r_w^j)$	Interdependency coefficient from the j-th critical infrastructure to the i-th critical infrastructure when $q_j \in r_w^j$

Abbreviations

AIC	*Akaike Information Criterion*
BIC	*Bayesian Information Criterion*
CDF	*Cumulative Distribution Function*
CI	*Critical Infrastructure*
DIIM	*Dynamic Inoperability Input-output Model*
EVT	*Extreme Value Theory*
KLE	*Karhunen–Loève Expansion*
NH	*Natural Hazard*
PIT	*Probability Integration Transform*
PN	*Power Network*
RCP	*Representative Concentration Pathway*
RMSE	*Root-Mean-Square Error*
SF	*Stochastic Field*
SoS	*System of Systems*
WN	*Water Network*

1. Introduction

Natural hazards (NHs) such as floods, storms, droughts and heatwaves can severely impact Critical Infrastructures (CIs) operability [1], causing significant societal and economic damages [2,3]. Analyzing how NHs can affect CIs operability can provide knowledge relevant to inform the decision making of disaster risk managers and long-term infrastructure planners [4,5].

In recent years, NHs have been further exacerbated by climate change, with the associated increase of their frequency, intensity and spatial extent [6 - 8]. Considering only historical records for characterizing the exposure of CIs to NHs, thus, undermines the coverage of any prospective analysis with respect to scenarios triggered by future climatic conditions more severe than in the past [9]. Forward-looking, climate-driven scenarios must, thus, capture potential operability losses under changing NH conditions [10], to avoid risk underestimation [11, 12].

Different approaches have been developed to model the NH dynamics under climate change, namely physics-based hazard models and statistical approaches [13, 14]. Physics-based hazard models are high-fidelity models, whose results are useful for scenario-based assessment. For example, in [15], EURO-CORDEX regional climate models are used to evaluate the increase of river flood frequency and magnitude across Europe. At a local

scale, in [16], an inundation model is used to assess flood risk in central Italy, and in [17] a two-dimensional hydraulic model is used to explore flood extents under Representative Concentration Pathways (RCPs) 4.5 and 8.5, which describe intermediate and high greenhouse gas forcing scenarios, respectively [18]. However, all the modeling approaches used for the above analyses are computationally expensive, hazard-specific, and need a large amount of high-quality local data, which limits their scalability and generalization across regions and hazard types [19]. Statistical approaches do not model the NH physical process but catch its stochastic characteristics [20, 21]. For example, in [22 - 26], Extreme Value Theory (EVT) is used to estimate changing return levels of precipitation [22 - 24], floods [25] and wind [26] considering also climatic covariates to capture non-stationarity. Despite this, EVT overlooks spatial dependencies and cross-correlation among locations, which are instead relevant when the aim is to assess cascading effects in the System of Systems (SoS) made of multi-state interdependent CIs, because failures at spatially correlated locations can occur simultaneously, amplifying disruption cascade propagation throughout the interdependencies of the CIs. Recent studies have highlighted that even when detailed flood hazard modeling is available, the lack of integrated probabilistic frameworks capable of considering the stochastic process of cascade propagation of hazard-induced failures through the CIs limits the assessment of indirect impacts on critical services [27]. When the risk assessment concerns geographically distributed assets within the SoS, EVT, thus, loses its effectiveness [28].

Copula-based methods can be used to model multivariate hazard dependencies and spatially coherent hazard patterns of NHs. For example, in [29], Fisher copula is used to characterize spatial dependence of floods across catchments; in [30] a set of combined copula models are developed to model climate projections and evaluate changing flood characteristics in Iran across historical, mid-term and long-term future periods; in [5], a Canonical-vine copula is applied to capture spatial dependence of wind gusts in Northeast Italy and integrate hazard scenarios into a Dynamic Input-output Inoperability Model (DIIM) for assessing the impact of cascading effects on interdependent power and gas CIs. Nevertheless, applying copula models to high-dimensional spatial domains is computationally demanding and particularly sensitive to uncertainties in copula structure selection and parameter estimation [31].

Stochastic Field (SF) methods are well established in civil and structural engineering for modeling spatial variability and loads [32 - 34], and offer a promising alternative for generating climate-aware hazard scenarios that are spatially coherent and computationally efficient [35]. SF can be generated by Karhunen–Loève Expansion (KLE), whose spectral decomposition can approximate a random field through covariance-based orthogonal expansions and preserves spatial dependence while reducing the computational demand [36]. By combining mathematical rigor with a computationally tractable solution, SF

provides a scalable framework for integrating climate projections into hazard analyses. To the authors' knowledge, SF application for NHs risk assessment of interdependent CIs exposed to climate change has not yet been explored: existing studies [37, 38] focus on direct damage to single assets, whereas the complexity of analyzing interdependent CIs has not been addressed.

In this work, we propose an original modeling framework that uses SF for climate change-dependent NH modeling within a DIIM framework [39] to assess the inoperability of multi-state interdependent CIs when exposed to NH-triggered scenarios. The framework is developed in such a way that open-access available global datasets (e.g., Copernicus Climate Data Store [40], NASA repositories [41], EURO CORDEX repository [42]) can be used to build the SF ensuring transferability of the approach across different spatial regions.

The novel contributions of the research presented in this paper are: (*i*) the development of a SF framework capable of generating spatially coherent hazard scenarios, thereby advancing hazard modeling by preserving spatial dependencies in a computationally efficient manner; (*ii*) the integration of climate change projections to assess evolving hazard intensities and spatial patterns, while relying exclusively on open-access datasets to ensure feasibility and transferability across diverse geographical contexts; (*iii*) the integration of spatially coherent NH scenarios in a multi-state, interdependent CI inoperability assessment model, enabling the analysis of cascading effects from a SoS perspective and providing insights into CIs inoperability under climate-induced NHs.

The remainder of this paper is organized as follows. Section 2 presents the proposed methodology for generating spatially correlated hazard scenarios using SF and integrating them into the inoperability assessment model of multi-state interdependent CIs. Section 3 describes the case study and data sources. Section 4 discusses the results and Section 5 concludes with remarks on the contributions, limitations and directions for future research.

2. Modeling Framework

The proposed modeling framework consists of three modules, as shown in Figure 1: (*i*) SoS and NH characterization, (*ii*) SF hazard scenario generation, and (*iii*) Inoperability assessment of multi-state interdependent CIs.

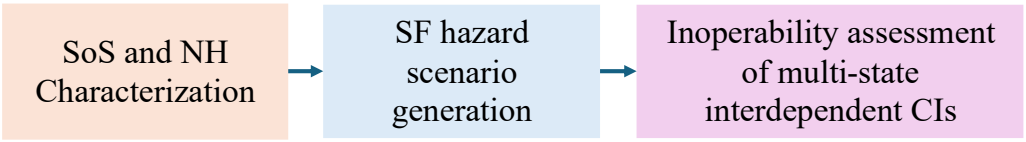

Figure 1. Modeling framework

2.1 SoS and NH characterization

In general terms, NHs can be described by one (or more) characteristic variables $H^* \in \mathcal{H} = \{H_1, H_2, \dots, H_h\}$: windstorms, for example, by wind speed or wind gust, floods by water depth, snowstorm by snow load, etc. [43]. A selected characteristic variable $H^* \in \mathcal{H}$ is here modeled as a spatio-temporal field $H^*(\bar{d}, t)$, where $\bar{d}_l = (longitude, latitude) \in \mathcal{D}$ denotes the spatial location within the study region and $t \in \mathcal{T}$ denotes time within the horizon of analysis. Records of $H^*(\bar{d}, t)$ are collected from freely available datasets, such as the Copernicus Climate Data Store [40], NASA repositories [41] and national meteorological agencies databases [44]. These data are required to cover the spatial domain $\mathcal{D}$ and the temporal horizon $\mathcal{T}$, ensuring that both the CI assets and the geographical footprint of the selected natural hazard are well covered.

The study region, i.e., the geographical area where CIs and NHs interact, is here defined as $\mathcal{D} \subset \mathbb{R}^2$. A SoS composed of M interdependent CIs is considered within $\mathcal{D}$. Each i-th CI is modeled as a direct graph $G^i \equiv (N^i, E^{(i,i)})$, where N^i denotes the set of nodes (e.g., substations, pumping stations) and $E^{(i,i)}$ the set of intra-system connections (e.g., transmission lines, distribution pipes) also called edges. The state of each element of a CI, whether node or edge, can evolve across multiple performance levels, from fully operational to degraded and, then, failed. Interdependencies between different CIs are represented by inter-graph connections $E^{(i,j)}$, which capture functional dependencies between G^i and G^j. Further details on the CI modeling approach can be found in [39].

Climate projections that describe the future evolution of hazard frequency and intensity are selected from established archives and are driven by RCPs, comprising four standardized greenhouse gas concentration trajectories (RCP2.6, RCP4.5, RCP6.0 and RCP8.5) constructed to span low, intermediate and high forcing futures [45]. In practical terms, RCP2.6 describes a scenario of strong mitigation of greenhouse gas emissions with declining concentrations after mid-century; RCP4.5 and RCP6.0 represent stabilization at intermediate levels of greenhouse gas emissions; RCP8.5 represents a future of high concentration pathway. RCPs are scenario inputs used to drive climate-model experiments, i.e., numerical simulations in which prescribed greenhouse gas concentration trajectories force global or regional climate models to generate future climate projections [46].

A temporal resolution Δ_t and a spatial resolution Δ_s are to be selected to match the hazard dynamics (e.g., daily for wind gusts or snow load; hourly for thermal stress or short-duration hydrologic responses), and to grasp the distance between adjacent CI assets, respectively. For example, in ERA5 data from Copernicus the spatial resolution is typically $\Delta_s \approx 25$ km [47], whereas for EURO-CORDEX dataset it is $\Delta_s \approx 11$ km [42].

To ensure consistency across present and future conditions, historical records and climate projections are harmonized to the same spatial domain $\mathcal{D}$ and target resolution (Δ_t, Δ_s). Hazard datasets are pre-processed for clean up from missing and/or corrupted values: missing values are reconstructed by nearest-neighbor or carry-forward methods to preserve continuity [48], whereas corrupted, physically implausible values (e.g., negative depths, zero gusts at active stations, sensor saturation) are removed if out of site- and season-specific plausibility bounds. The outcome is a cleaned spatio-temporal series $H^*(\bar{d}, t)$ consistently defined over $\mathcal{D} \times \mathcal{T}$. Figure 2 summarizes the steps of the modeling module 1.

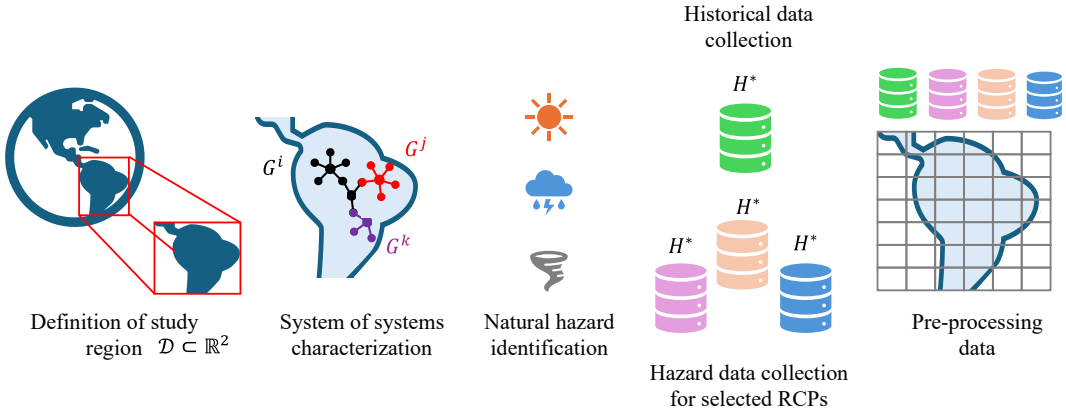

Figure 2. SoS and NH characterization

2.2 SF hazard scenario generation

To generate a stochastic hazard field whose values are realistic at each site and whose spatial dependence matches the data, it is necessary to: (*i*) capture site-specific behavior by fitting a marginal distribution at each location; (*ii*) obtain a spatial correlation among locations by removing the marginal effects via the Probability Integration Transform (PIT); and (*iii*) simulate a spatially coherent field with KLE using the fitted marginals and the correlations.

(i) To capture site-specific behavior (independently of spatial dependence), we fit a parametric marginal distribution from a set of candidates $\mathcal{F} = \{\mathcal{F}_p\}$ (e.g., Lognormal, Weibull, Gamma) at each location $\bar{d}_l \in \mathcal{D}$. The fitting is performed on the series of records $\{H^*(\bar{d}_l, t) | t \in \mathcal{T}_E\}$, where $\mathcal{T}_E \subset \mathcal{T}$ denotes

the set of time instants for which the hazard intensity exceeds a prescribed threshold $\tau \in \mathbb{R}^+$ at least at one spatial location within the domain, i.e.

$$\mathcal{T}_E = \left\{ t \in \mathcal{T} : \max_{\bar{d}_l \in \mathcal{D}} H^*(\bar{d}_l, t) \geq \tau \right\} \quad (1)$$

For each candidate distribution $\mathcal{F}_p$, the parameters $\theta_{l,p}$ are estimated by maximum likelihood estimation,

$$\theta^*_{l,p} = arg\max_{\theta} \ \mathcal{L}\left(\left\{ H^*(\bar{d}_l, t) \right\}_{t \in \mathcal{T}_E} \middle| \mathcal{F}_{p,} \theta \right) \quad (2)$$

where $\mathcal{L}(\cdot)$ denotes the likelihood function. The marginal model selection can be based on information criteria, such as the Bayesian Information Criterion (BIC) [49] or the Akaike Information Criterion (AIC) [50]. The marginal distribution selected at $\bar{d}_l$ is $\mathcal{F}_l(\cdot) = \mathcal{F}_{\mathcal{F}_{p_l^*}}\left(\cdot \middle| \theta^*_{l,p_l^*} \right)$, where p_l^* denotes the index of the candidate minimizing the BIC.

The adequacy of the selected marginal can be, then, assessed using goodness-of-fit diagnostics, including the Kolmogorov-Smirnov test [51], complemented by Anderson-Darling tests [52] and quantile-quantile plots [53].

(ii) To model spatial dependence, PIT can be used to map observations on a common uniform scale and preserves their rank structure [54]: for each $t \in \mathcal{T}_E$ and location $\bar{d}_l \in \mathcal{D}$, the PIT is:

$$u_l(t) = \mathcal{F}_l\left(H^*(\bar{d}_l, t) \right) \in [0,1] \quad (3)$$

The uniform variables $u_l(t)$ are, then, mapped to a Gaussian scale through a Gaussian anamorphosis (probit transform),

$$Z_l(t) = \Phi^{-1}(u_l(t)), \quad t \in \mathcal{T}_E, \bar{d}_l \in \mathcal{D} \quad (4)$$

where Φ is the standard normal cumulative distribution function.

For each site l, the resulting Gaussian scores $\{Z_l(t)\}_{t \in \mathcal{T}_E}$ are centered by subtracting their empirical mean over $\mathcal{T}_E$, so that they have zero mean. This centering step removes residual location-specific offsets and ensures that spatial dependence is characterized solely through second-order statistics.

Spatial dependence is, then, inferred on this common Gaussian scale using the centered Gaussian scores $Z_l(t)$: for two locations $\bar{d}_l$ and $\bar{d}_o$ with latitude ϕ_l, ϕ_o and longitudes ψ_l, ψ_o (in radians), the sample correlation between the

corresponding centered Gaussian score time series $Z_l(t)$ and $Z_o(t)$ is computed. These pairwise correlation estimates are, then, grouped into distance classes according to the inter-site distance h_{lo}, i.e., the haversine great-circle distance [53], in Equation (5), yielding an empirical correlogram,

$$h_{lo} = 2r_E \sin^{-1}\left(\sqrt{sin^2\frac{\phi_l - \phi_o}{2} + \cos\phi_l + \cos\phi_o sin^2\frac{\psi_l - \psi_o}{2}}\right) \quad (5)$$

where $r_E = 6371$ km is the mean Earth radius.

Then, a parametric correlation function $\rho(h;\vartheta)$ (e.g., exponential, Gaussian, spherical, or Matérn) is fitted to the empirical correlogram by weighed least squares [56],

$$\vartheta^* = arg\min_{\vartheta} \sum_{b=1}^{B} \omega_b\left[\bar{\rho}_b - \rho(h_b;\vartheta)\right]^2 \quad (6)$$

where $(h_b, \bar{\rho}_b, \omega_b)$ are the bin-center distance, the average empirical correlation in bin b and the associated weight, respectively. These correlation families are standard in spatial statistics, with the Matérn class favored for its interpretable range and smoothness parameters [57].

As a summary measure of fit, the root-mean-square error (RMSE) between the empirical correlogram and the fitted model can be adopted:

$$RMSE(\vartheta^*) = \sqrt{\frac{1}{B}\sum_{b=1}^{B}\left[\bar{\rho}_b - \rho(h_b;\vartheta^*)\right]^2} \quad (7)$$

(iii) Since the Gaussian scores $Z_l(t)$ have unit variance by construction, their covariance matrix coincides with the correlation matrix [58, 59]. Evaluating the fitted correlation function $\rho(\cdot;\vartheta^*)$ at all inter-site distances h_{lo}, thus yields the target correlation (and hence covariance) matrix $\bar{\bar{C}}(\vartheta^*) \in \mathbb{R}^{\mathcal{D}\times\mathcal{D}}$, with entries:

$$\bar{\bar{C}}_{lo} = \rho(h_{lo};\vartheta^*) \quad (8)$$

Let $\bar{\bar{C}} = V\Lambda V^{\mathrm{T}}$ denote its eigen-decomposition, where $\Lambda = \mathrm{diag}(\lambda_1, \dots, \lambda_d)$ with $(\lambda_1 \geq \cdots \geq \lambda_d \geq 0)$ and V contains the associated orthonormal eigenvectors [58]. The smallest integer k is selected such that a prescribed variance-retention level $\varsigma \in [0,1]$ (e.g., $\varsigma = 0.95$) is satisfied:

$$\frac{\sum_{v=1}^{k} \lambda_v}{\sum_{v=1}^{d} \lambda_v} \geq \varsigma \tag{9}$$

The KLE is, then, used to generate spatially coherent Gaussian fields [60] as:

$$\bar{Z}^s = V_{:,1:k} \Lambda_{1:k,1:k}^{1/2} \xi^s, \qquad \xi^s \sim \mathcal{N}\left(0, \bar{\bar{I}}_k\right) \tag{10}$$

where $V_{:,1:k} \in \mathbb{R}^{d \times k}$ contains the first k eigenvectors, $\Lambda_{1:k,1:k}$ is the diagonal matrix of the retained eigenvalues, $\xi^s \in \mathbb{R}^k$ is a vector of independent standard normal coefficients, and $\bar{\bar{I}}_k$ is the $k \times k$ identity matrix. This construction yields Gaussian fields whose spatial covariance matches $\bar{\bar{C}}(\vartheta^*)$, and provides an optimal (global mean-square) truncated representation once the covariance is specified [61].

Finally, we recover the physical hazard values to consider for the scenario simulation, by inverse transform at each site:

$$u_l^s = \Phi(Z_l^s), \qquad h_l^s = F_l^{-1}(u_l^s) \tag{11}$$

where Φ is the standard normal cumulative distribution function. Collecting scalars across $\mathcal{D}$ gives the vector $\bar{h}^s = [h_1^s, \dots, h_d^s]^T$. The ensemble $S = \{\bar{h}^1, \dots, \bar{h}^S\}$ is, then, a stochastic, spatially coherent set of hazard scenarios consistent with the event-focused marginals and the estimated spatial dependence, where each $\bar{h}^s$ contains the hazard intensity h_l^s at each location $\bar{d}_l$ of the SoS. An overview of the SF generation pipeline is shown in Figure 3.

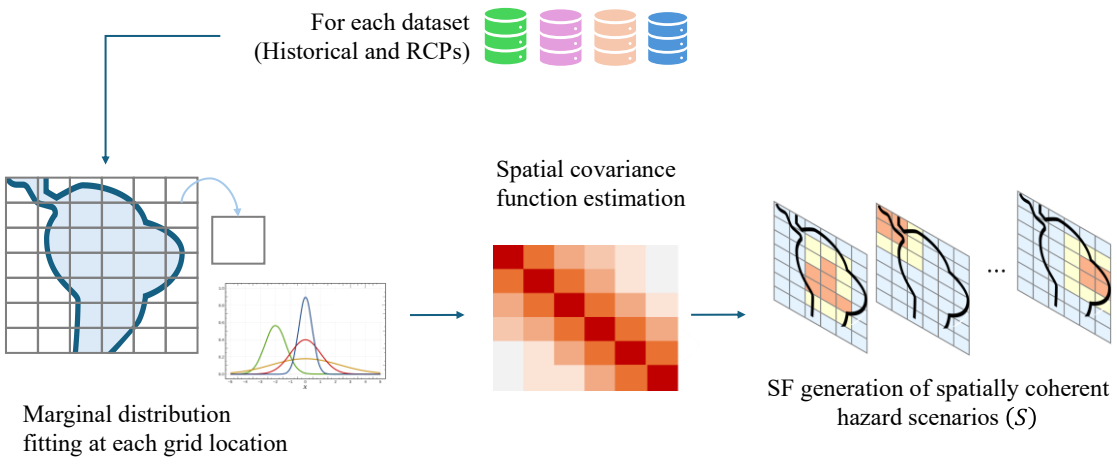

Figure 3. SF hazard scenario generation

2.3 Inoperability assessment of multi-state interdependent CIs

CI inoperability is evaluated with a multi-state DIIM [39]. The evolution of inoperability across the M interdependent CIs of the SoS is given by:

$$\bar{q}(t+1) = \bar{q}(t) - \bar{\bar{K}}\bar{q}(t) + \bar{\bar{K}}\bar{\bar{A}}(t)\bar{q}(t) + \bar{\bar{K}}\bar{c}(t) \tag{12}$$

where $\bar{q}(t) \in [0,1]^M$ is the inoperability vector (0 = fully operational, 1 = fully inoperable); $\bar{c}(t)$ is the exogenous perturbation vector (typically $\bar{c}(0)$ from the hazard impact and $\bar{c}(t>0) = 0$); $\bar{\bar{K}} = diag(k_1, \dots, k_M)$ is the diagonal $M \times M$ recovery matrix; $\bar{\bar{A}}(t)$ is the multi-state interdependency matrix. Entry $a_{ji}(t)$ quantifies the fraction of functionality that the j-th CI loses per unit inoperability of the i-th CI at time t (with $a_{ii}(t) = 0$).

To estimate the interdependency coefficients, we implement the data-driven approach introduced in [39], using the ensemble of hazard pseudo-scenarios generated via SF to characterize cascading effects.

For each SF realization $\bar{h}^s$, the CI elements hit by the NH are identified: nodes are considered exposed to the NH intensity at their location, whereas edges (that span over multiple locations) are conservatively considered exposed to an equivalent hazard intensity defined as the maximum intensity encountered along its footprint,

$$h^s_{e^{(i,i)}_{op}} = max\left(h^s_1, h^s_2, \dots, h^s_y\right) \tag{13}$$

Element-level damage is, then, evaluated through component-specific fragility functions, which relate the hazard intensity to the probability of exceeding discrete performance states. Nodes and edges are each characterized by ordered sets of performance states ranging from full operability to complete failure. Assuming, without loss of generality, a fragility of lognormal form, the probability that a given element reaches or exceeds a damage state is computed as

$$\mathbb{P}\left(x^i_{z,f} \middle| h^s_l\right) = \Phi\left(\frac{ln(h^s_l) - \mu_{z,f}}{\beta_{z,f}}\right) \tag{14}$$

$$\mathbb{P}\left(x^i_{e^{(i,i)}_{op},u} \middle| h^s_{e^{(i,i)}_{op}}\right) = \Phi\left(\frac{ln\left(h^s_{e^{(i,i)}_{op}}\right) - \mu_{e^{(i,i)}_{op},u}}{\beta_{e^{(i,i)}_{op},u}}\right) \tag{15}$$

where Φ is the standard normal cumulative distribution function, $x^i_{z,f}$ is the f-state of

node n_z^i, $x^i_{e_{op}^{(i,i)},u}$ is the u-state of edge $e_{op}^{(i,i)}$, h_l^s is the node scenario intensity, $h^s_{e_{op}^{(i,i)}}$ is the edge equivalent intensity from Equation (13), and μ, β are the fragility parameters for the indicated element and state, respectively.

Based on these probabilities, binary or multi-state sampling is applied [5] to assign each element a discrete damage state for the given scenario.

Element-level damage states are aggregated to obtain infrastructure-level degradation. For each i-th CI, the infrastructure performance is represented by a discrete set of ordered states $\bar{X}^i = \{X_0^i, X_1^i, \dots, X_L^i\}$, (where X_0^i corresponds to the perfect functioning of the CI, and X_L^i to complete failure). The infrastructure state depends on the configuration of damaged elements and is determined through a structural mapping $X_l^i = \phi\left\{\bar{x}^{n_1^i}, \bar{x}^{n_2^i}, \dots, \bar{x}^{n_Z^i}, \bar{x}^{e_{12}^{(i,i)}} \dots\right\}$, with $\bar{x}^{(\cdot)}$ denoting the discrete performance states of each node or edge comprising the i-th infrastructure.

Having identified the infrastructure state, its operational performance can be quantified using a demand-based proxy. Specifically, the operational performance associated with state X_l^i is defined as:

$$O(X_l^i) = 1 - \frac{D(X_l^i)}{D(X_0^i)} \tag{16}$$

where $D(X_l^i)$ is the demand satisfied by the i-th infrastructure in state X_l^i, and $D(X_0^i)$ corresponds to the demand under perfect functioning. Thus, if $D(X_l^i) = D(X_0^i)$, the infrastructure is fully functional and $O(X_l^i) = 0$; if $D(X_l^i) = 0$, the infrastructure cannot satisfy any demand and $O(X_l^i) = 1$.

Repeating this process for the whole ensemble of hazard scenarios yields scenario-dependent inoperability values and associated cascading effects. These outcomes are used to empirically estimate interdependencies between infrastructures. For each dependency relation $i \to j$, the inoperability range $[0,1]$ of the i-th source CI is discretized into intervals $r^i = \{r_1^i, r_2^i, \dots, r_W^i\}$ and $r^j = \{r_1^j, r_2^j, \dots, r_B^j\}$ for the j-th dependent CI; then, conditional probabilities of the form

$$\mathbb{P}(q_j \in r_b^j \,|\, q_i \in r_w^i) \tag{17}$$

are estimated by counting occurrences across all scenario-time realizations. Interval-specific interdependency coefficients are, then, obtained through a probability-weighted aggregation,

$$a_{ji}(r_w^i) = \sum_{b=1}^{B} \mathbb{P}(q_j \in r_b^j \,|\, q_i \in r_w^i) \times ub(r_b^j) \tag{18}$$

where $ub(r_b^j)$ is the upper bound of interval r_b^j. Coefficients are bounded in [0,1]. At each time step t, the interdependency coefficients for the next update are selected based on the current inoperability of the source CIs: if $q_i(t-1) \in r_w^i$, then $a_{ji}(t) = a_{ji}(r_w^i)$ for all $j \neq i$. This yields an interval-dependent interdependency matrix consistent with the observed cascades and requires only counting over scenario-time instances to estimate the conditioning probabilities [39].

In this way, interdependencies are inferred directly from hazard-driven degradation patterns and reflect physically meaningful relationships for the study region, rather than ad-hoc assumptions. Because interdependency coefficients are estimated separately for each hazard dataset (historical observations and RCP-based projections), the framework enables direct comparison of present and future system performance using CI- and SoS-level inoperability metrics (e.g., distributions of peak inoperability and time-to-recovery). Spatial patterns of service loss are also identified, and critical elements are ranked to support the evaluation of preventive and mitigation strategies across RCPs. Figure 4 summarize the steps of this modeling module.

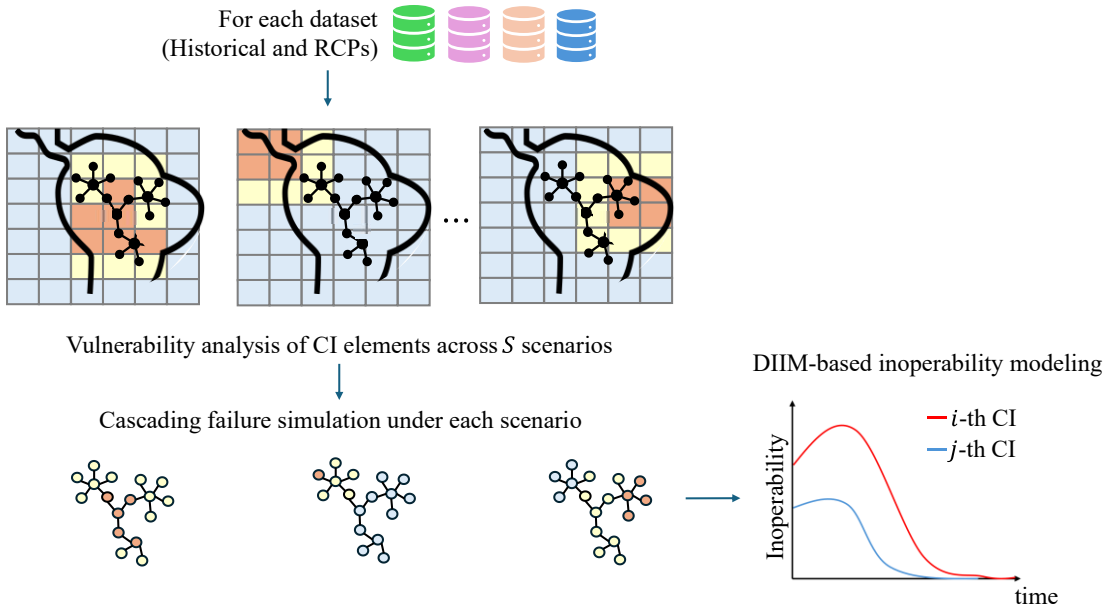

Figure 4. Inoperability assessment of multi-state interdependent CIs

3. Case study

The proposed framework is applied to a SoS composed of interdependent Power Network (PN) and Water Network (WN), originally introduced in [39]. In the present study, the

SoS is adapted to spatially locate it in North Italy, a region exposed to strong wind-gust events.

3.1 Description of study region and SoS (interdependent PN-WN)

The SoS is made of interdependent PN and WN assumed to be located in the Po River and pre-Alpine areas of North Italy, where wind-related NH can be significant [62]. Each CI is modeled as a directed graph, whose nodes represent physical assets and edges represent intra-system connections.

The PN (Figure 5 (a)) comprises 57 nodes and 80 transmission lines [63]. Nodes are categorized as generators or loads, according to their function. Generator nodes represent power-production units, load nodes represent substations or end-users. Through inter-system connections, the PN supplies the electrical power required to operate WN pumping and treatment facilities.

The WN (Figure 5 (b)) consists of 85 nodes and 84 pipes [64]. It includes a single generator node representing the main water-treatment facility, and 84 load nodes corresponding to pumping or distribution stations that deliver water to the demand sectors. The WN depends on electrical power for operation and, in turn, provides process/cooling water to all PN generation units through the corresponding inter-system connections.

Then, in the representative graph models of PN and WN, the interdependencies are modeled through directed inter-graph connections that represent the bidirectional functional relations between the two CIs. In the PN→WN direction, four PN nodes supply the single WN generator (1-out-of-4 redundancy); additionally, three PN nodes supply three WN nodes (without backup). For the WN→PN dependency, each PN generator is associated with two WN load nodes (redundant pairs) that provide the required water for cooling service. In Figure 5 (c) interdependency links are represented as directed black arrows connecting the corresponding nodes of the two networks. To facilitate reproducibility of the results, Appendix A details the dependency relations and specifies the nodes involved.

To characterize the NH affecting the SoS, the environmental variable H^* adopted in this case study is the daily maximum wind gust registered at a height of 10 meters above ground level, as this is internationally taken as representative of wind forcing relevant for impact assessment on exposed CIs [65].

Spatial and temporal characterization of H^* is derived from the EURO-CORDEX regional climate simulations [39], produced at a horizontal resolution of $0.11°$ ($\Delta_s \approx 11$

km) and covering the domain of North Italy:

$$\mathcal{D} \subset \mathbb{R}^2 = \{(\phi, \psi): \phi \in [43.7°, 47.2°], \psi \in [6.5°, 14.2°]\} \quad (19)$$

The discretization of $\mathcal{D}$ yields 1568 grid points, each corresponding to a spatial location $\bar{d}_l \in \mathcal{D}$. For each day $t \in \mathcal{T}$, the variable $H^*(\bar{d}_l, t)$ represents the maximum value of 3-second gust recorded at that grid point. The historical dataset covers the available period $\mathcal{T} = [t_0, t_f]$ =[1 Jan 1970, 31 Dec 2005], with a temporal resolution Δ_t= 1 day, resulting in $|\mathcal{T}| = 13{,}149$ consecutive time steps. This provides a continuous spatiotemporal record of wind gust intensity at all grid points of $\mathcal{D}$.

To assess the effects of climate change on the NH of wind gust and the related cascading impacts associated to the daily maximum wind gust at 10 m height, projections from EURO-CORDEX are considered, derived from the MPI-ESM-LR→SMHI-RCA4 model chain, and covering RCP 4.5 and RCP 8.5 [39]. These RCPs represent intermediate-stabilization and high-forcing future scenarios, respectively. Datasets are provided on the EUR-11 grid (~0.11° resolution), which is consistent with the spatial discretization adopted in the historical analysis and has been shown to reproduce realistic wind extremes over Europe [66, 67].

The temporal window of analysis considers: (*i*) Near-term (2006-2040), (*ii*) Mid-century (2041-2070) and (*iii*) Late-century (2071-2100). All datasets consider the same grid spacing (Δ_s), temporal step (Δ_t) and study domain ($\mathcal{D}$) used in the historical dataset to ensure methodological continuity.

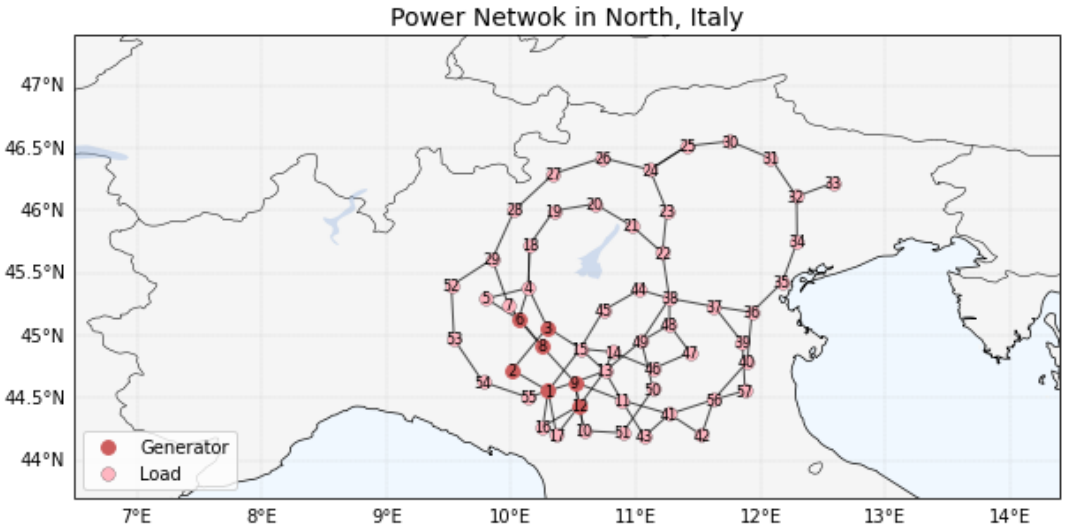

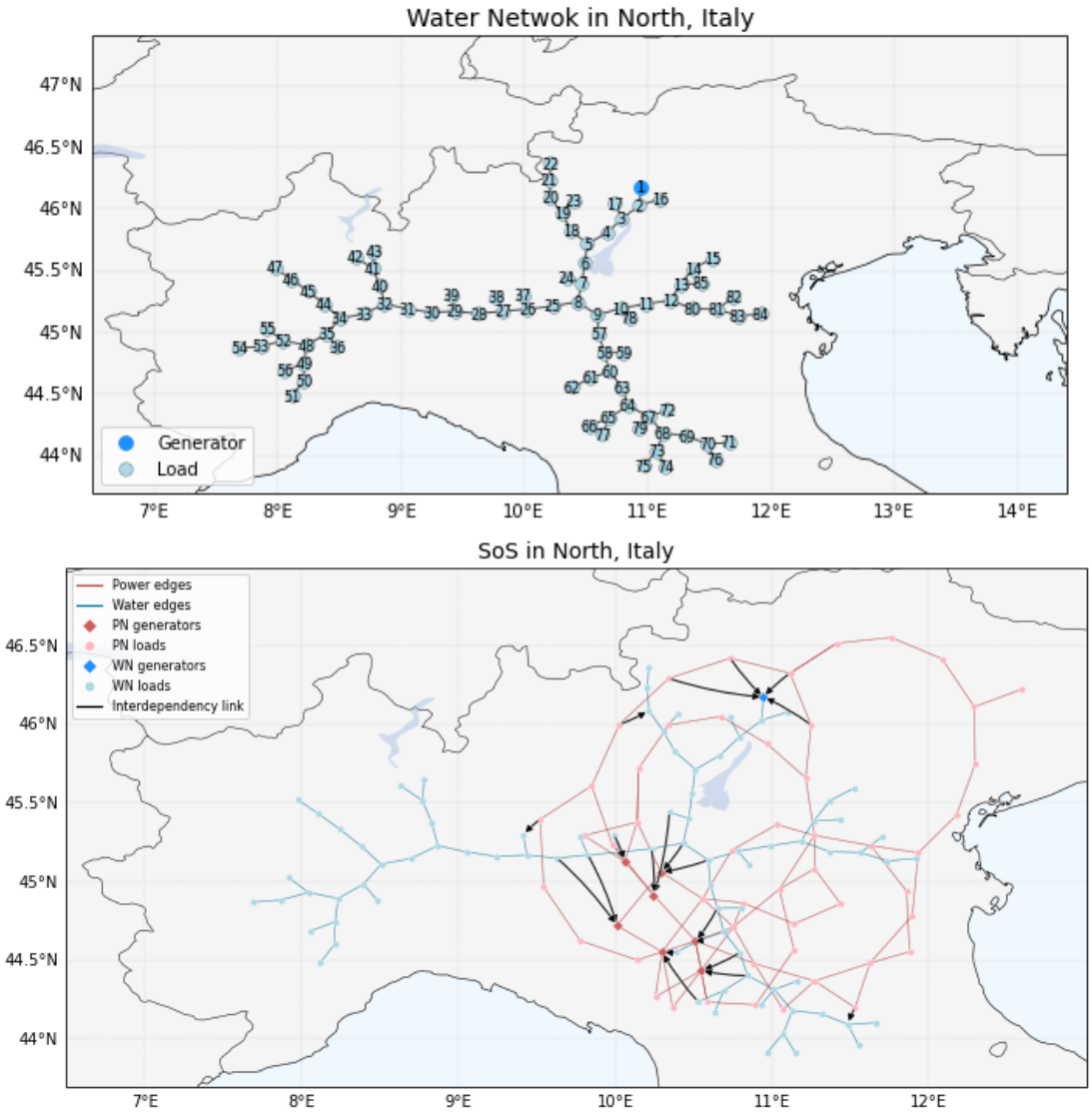

Figure 5. SoS in the North Italy

Figure 6 presents boxplots of exceedance magnitudes $\{H^*(\bar{d}_l, t) | t \in \mathcal{T}_E\}$ for each RCP and period, with markers indicating the mean, 95th and 99th percentiles, and annotations showing the number of occurrences of extreme gusts with intensities above 50 ms^{-1}. The median and interquartile ranges remain nearly unchanged across time windows and between RCPs, suggesting limited intensification in the typical and upper-tail gust magnitudes. However, the counts exceedingly above 50 ms^{-1} increase notably under RCP 8.5, particularly in the late-century period, indicating that future changes are driven more by the rising frequency of extreme gusts rather than by a substantial shift in their intensity.

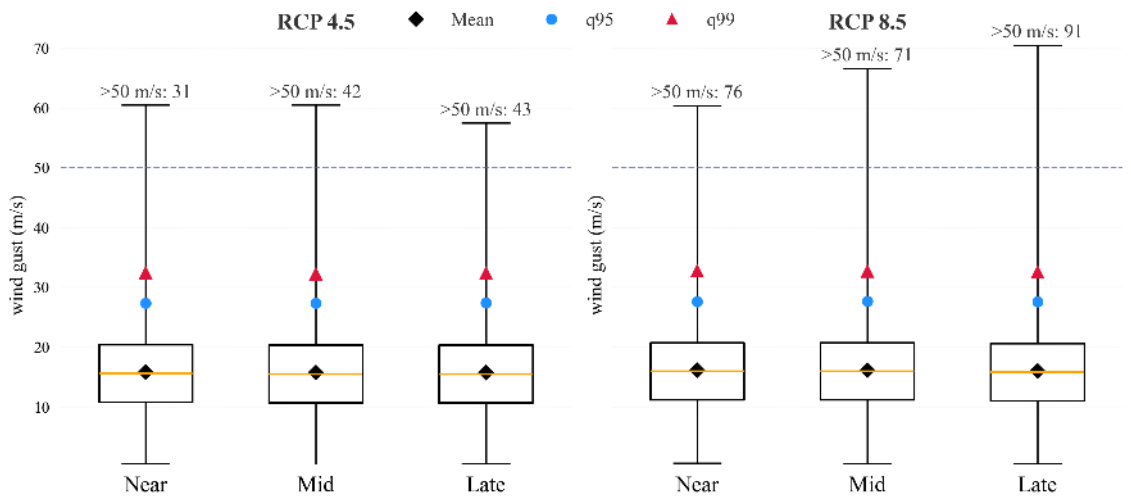

Figure 6. Distribution of projected wind gust extremes under RCP 4.5 and RCP 8.5

3.2 SF generation of wind-hazard scenarios

The subset $\mathcal{T}_E$ (Equation (1)) is constructed retaining all days on which at least one grid point in $\mathcal{D}$ exceeds the physical critical threshold $\tau = 30$ ms^{-1}, that is here considered as wind gust speed capable of stressing or damaging CI elements, as argued in [68 - 70]. For the historical period ($\mathcal{T}$ =[1 Jan 1970, 31 Dec 2005]), $\mathcal{T}_E$ results in 2707 days which are fully characterized for all the 1568 grid points.

At each grid point $\bar{d}_i \in \mathcal{D}$, $\{H^*(\bar{d}_i, t) | t \in \mathcal{T}_E\}$ is modeled using three distribution types $\mathcal{F} = \{\text{Weibull}, \text{Lognormal}, \text{Gamma}\}$. Parameters are estimated by maximum likelihood as in Equation (2) and the optimally fitting type is selected following the criteria described in Section 2.2. For the historical dataset, the distribution of the best-fit marginal families (Figure 7) shows that $\mathcal{F}_l$ captures the local statistical behavior of wind-gust independently of spatial dependence: Weibull distribution is the best fitting (95.47% of the grid points); characterizing at best the wind regime over the Po Valley and surrounding plains; Lognormal is the best fitting for 1.02% of the grid points, mainly located in the pre-Alpine areas, where complex terrain and orographic channeling introduce large variability in gust intensities; Gamma is the best fitting for 3.51% of the grid points mainly located along the coast and the southern region, where mixed wind regimes and intermittent gust events are common.

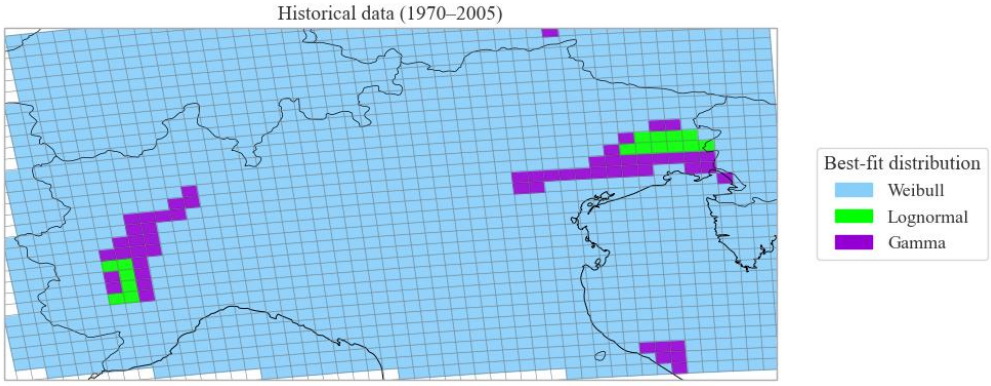

Figure 7. Spatial distribution of best-fit marginal families for wind-gust data (historical period)

The procedure is applied for each future time window using the climate projections. The balance among the fitted distributions is similar to that of the historical case (Figure 8): Weibull dominates, Lognormal appears sporadically, a small increase of Gamma is observed for the mid- and far-future periods, most notably under RCP 8.5. Appendix B shows site-level fits (plain, foothill, pre-Alpine).

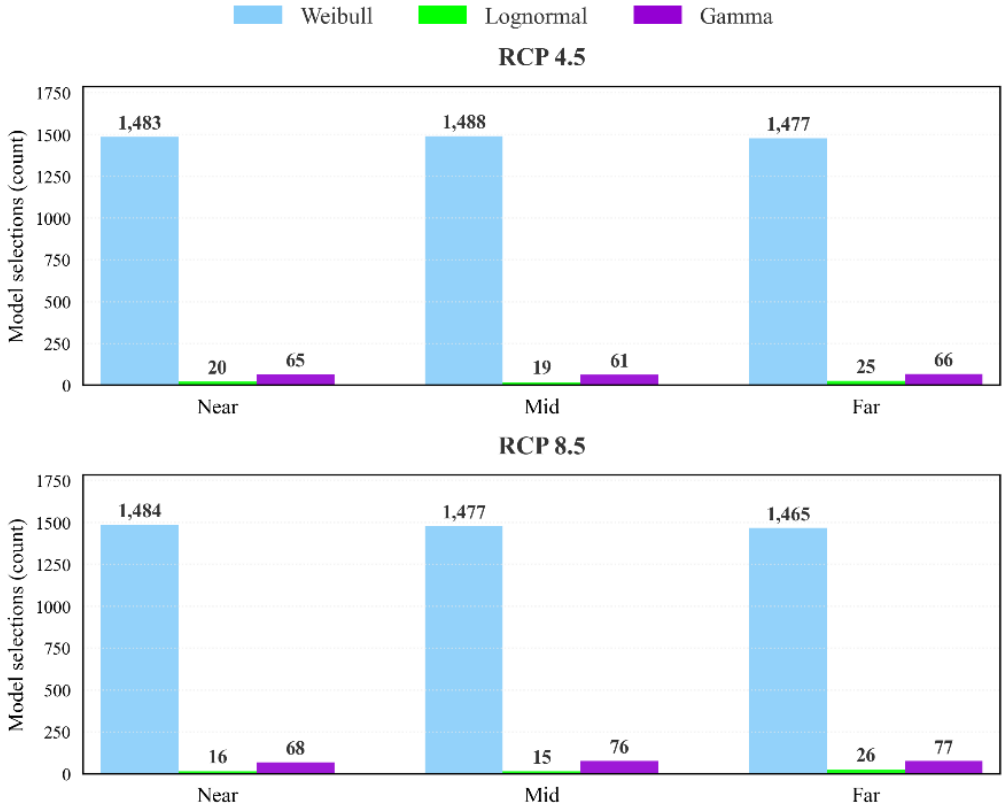

Figure 8. Count of best-model selection by RCP and period

To capture cross-site dependence, marginal effects are removed through the PIT and Gaussian anamorphosis (Equations 3 and 4), obtaining standardized Gaussian scores $Z_i(t)$. For the historical period, the empirical correlogram of $Z_i(t)$ (Figure 9) is computed

using 60 distance bins ($\approx 10-15$ km), resolving spatial correlation from grid scale up to the domain extent ($\sim$ 700 km). Four parametric kernels $\rho(h;\vartheta)$ have been considered for fitting, whose results are summarized in Table I and shown in Figure 9 (Exponential: purple, Gaussian: grey, Matérn: black, Spherical: blue).

Among these, the Matérn model provides the best fit (RMSE = 0.0234). The estimated range (~345 km) is consistent with synoptic-scale windstorms affecting large portions of the Po Valley and adjacent foothills, whereas the low smoothness parameter reflects the rough, intermittent nature of gust fields driven by convection, orographic channeling and land-sea contrasts. The nugget term (≈ 0.30) indicates substantial sub-grid or microscale variability, explaining why correlations do not reach unity at very short distances. In contrast, the exponential and Gaussian models differ in how they reproduce the observed decay: the exponential kernel captures the initial drop but slightly underestimates correlation persistence at intermediate distances, whereas the Gaussian kernel remains too flat at short lags and, then, decay too rapidly beyond $\sim$ 200 km, reflecting an overly smooth behavior near the origin and a loss of long-range correlation. The spherical kernel declines too quickly to near-zero after $\sim$ 500 km and cannot reproduce the long-lag tail, yielding a large RMSE. Overall, the Matérn kernel captures the observed smooth decay from $\sim$ 0.9 at very short lags to near-zero by $\sim$ 700 km, while accommodating the rough, intermittent nature of gust fields; this justifies using it to build the covariance for KLE.

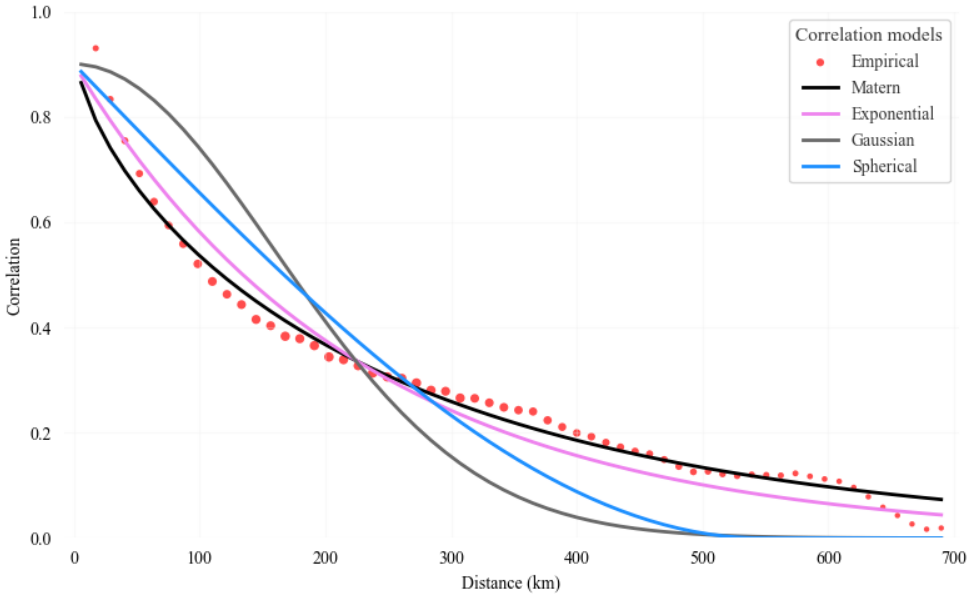

Figure 9. Empirical correlogram and fitted spatial correlation models for wind gust (historical data)

Table I. Parameters and RMSE of fitted spatial correlation models wind gust (historical data)

Model	Range (km)	Smoothness	Nugget	RMSE

Exponential	229	NA	0.1	0.0413
Gaussian	226	NA	0.1	0.1398
Matérn	345	0.058	0.3	0.0234
Spherical	546	NA	0.1	0.0953

The dependence modeling procedure is also applied to each future time window of climate projections. The Matérn kernel remains the preferred model for all scenarios, with RMSE values comparable to the historical dataset (Table II, Figure 10). Under RCP 4.5, spatial parameters remain nearly stationary (ranges ≈ 336-378 km; smoothness ≈ 0.06-0.08; nugget = 0.3; RMSE ≈ 0.023-0.026), whereas RCP 8.5 shows slightly stronger medium-to-long range dependence (≈200-600 km), reflected in larger ranges (396-424 km) and smoother behavior (≈0.09-0.1). Overall, the future gust field preserves short-lag roughness while exhibiting modestly increased spatial coherence under stronger forcing.

Table II. Matérn parameters and RMSE under RCP 4.5 and 8.5

RCP	**Period**	**Model**	**Range (km)**	**Smoothness**	**Nugget**	**RMSE**
RCP 4.5	Near	Matérn	378	0.066	0.3	0.0234
	Mid	Matérn	336	0.057	0.3	0.0236
	Late	Matérn	349	0.079	0.3	0.0258
RCP 8.5	Near	Matérn	396	0.086	0.3	0.0261
	Mid	Matérn	406	0.1	0.3	0.0297
	Late	Matérn	424	0.1	0.3	0.0308

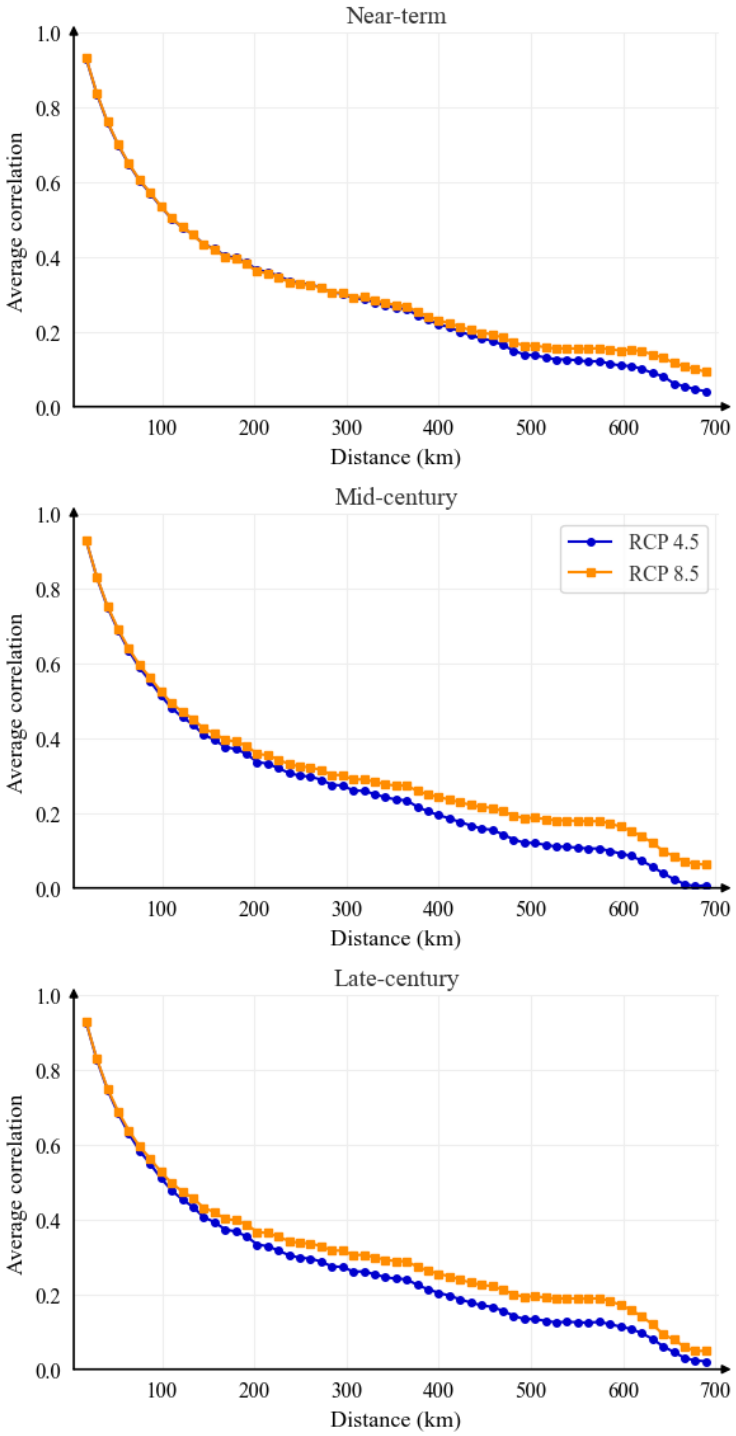

Figure 10. Correlograms of standardized wind gust fields for each RCP and period

Based on the fitted marginals and spatial parameters, the covariance matrix $\bar{\bar{C}}(\vartheta^*)$ is eigen-decomposed and truncated using a variance-retention level of $\varsigma = 0.95$. The resulting reduced KLE basis retains $k = 1026$ for the historical dataset, $k = 1036 - 1084$ under RCP 4.5, and $k = 1086 - 1117$ under RCP 8.5, consistent with the high

spatial resolution and slowly decaying spectrum typical of wind-gust fields in complex terrain [71]. Gaussian coefficients are sampled and mapped back to physical units to generate $S = 1000$ spatially coherent wind-gust scenarios for the historical period and for each RCP x period combination; an example of using historical data is shown in Figure 11, where also the PN nodes and edges are plotted. In this respect, it is worth mentioning that on what follows since wind gust affect overhead components, only the PN edges, i.e., transmission lines, are assumed to be directly exposed to the NH. The WN elements are not directly damaged by wind but may lose functionality because they depend on the PN for energy supply to pumping and control stations.

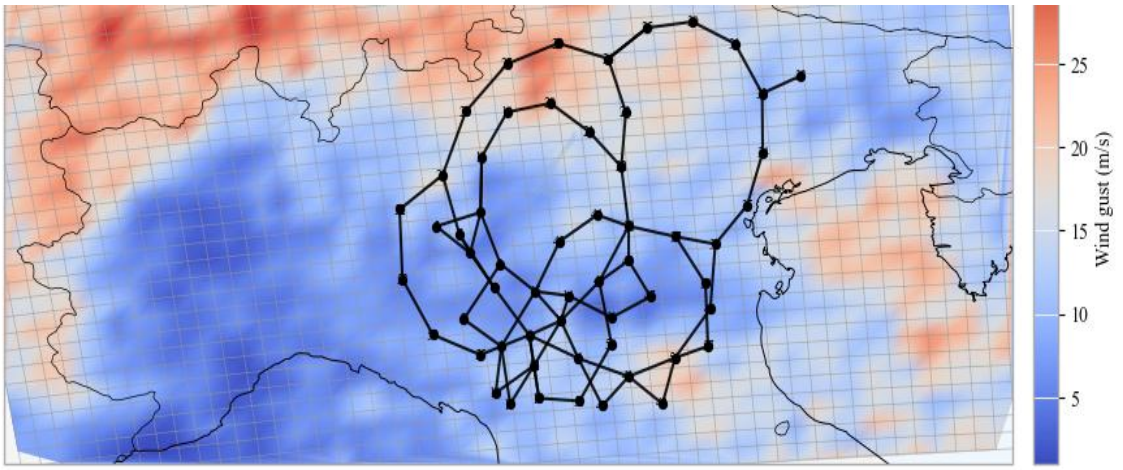

Figure 11. Example SF realization $\bar{h}^s$ of wind gust (based on historical dataset: 1970-2005)

Figure 12 presents representative realizations for RCP 8.5, illustrating the spatial coherence with the PN and the progressive intensification of the simulated gust fields across future periods.

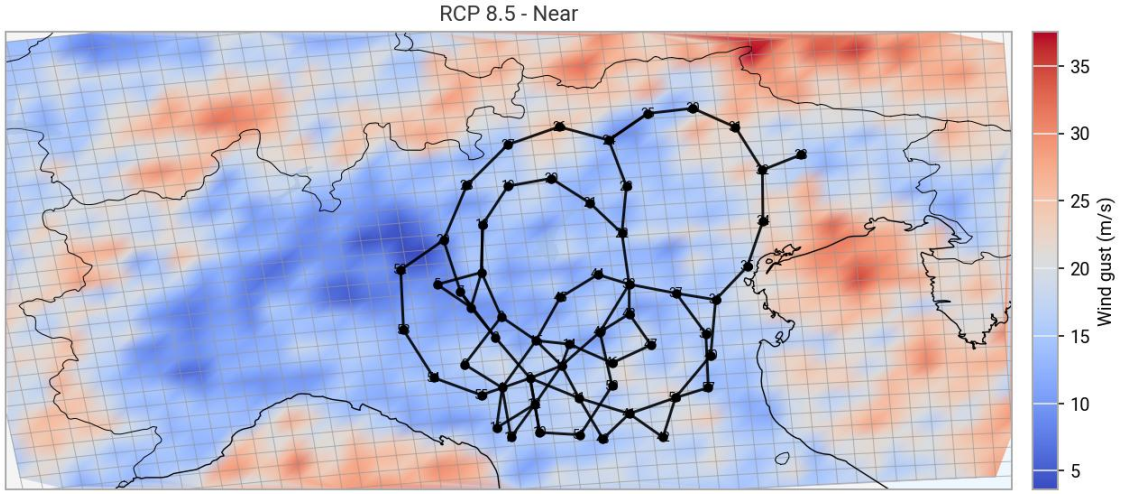

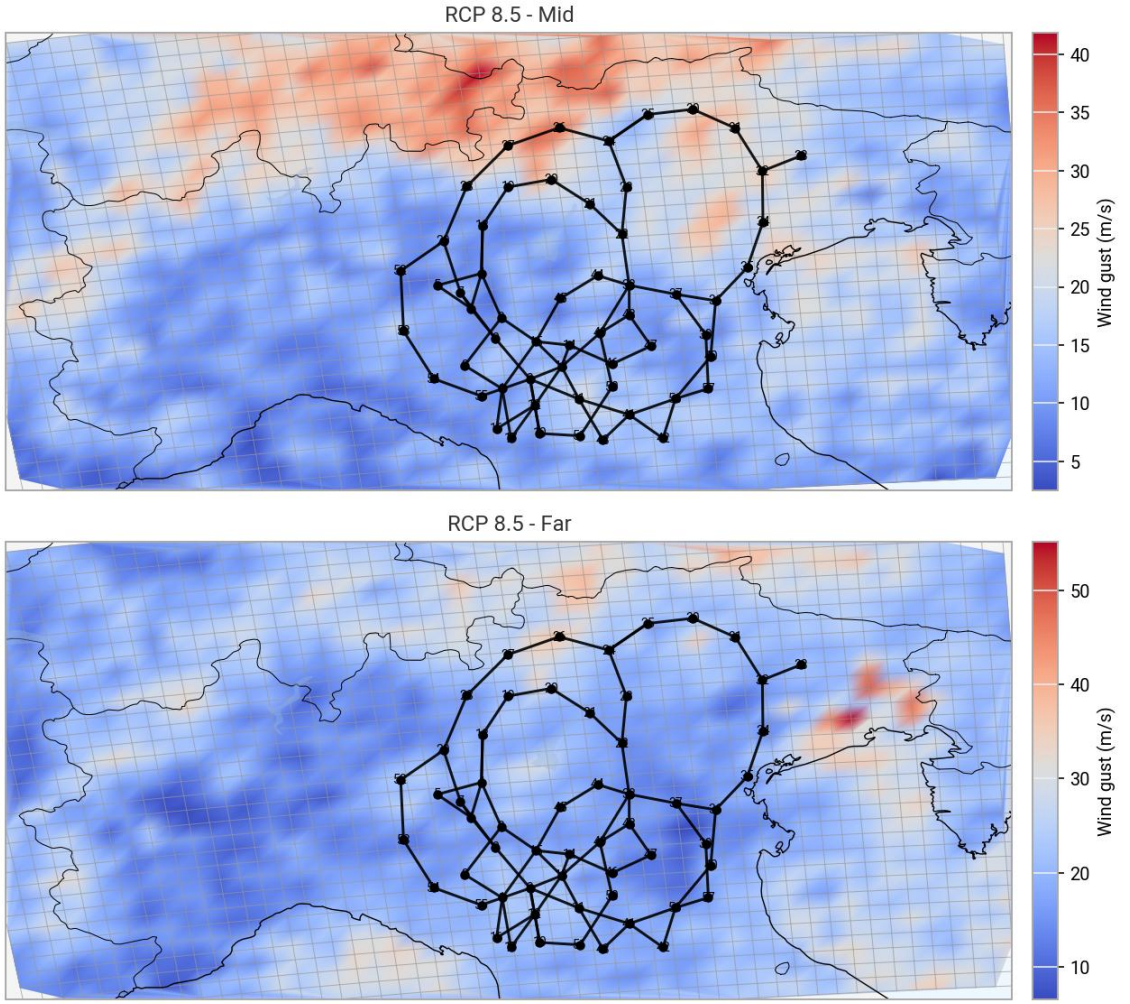

Figure 12. SF realizations of wind gust for the RCP 8.5 across near-, mid- and far-future periods

For validating the SF generated for the wind gust, the fidelity of the pseudo-generated hazard scenarios is assessed with respect to the original extreme event data $\mathcal{T}_E$ (Equation (1)), derived from historical dataset and climate projections under RCP 4.5 and 8.5. Validation serves to address whether: (*i*) the intensity of extreme events in the upper tail is accurately reproduced, and (*ii*) the spatial dependence structure of extreme events is preserved.

With respect to (*i*), Table III lists the RMSE at the 99th percentile between real and pseudo-generated fields for all cases considered (historical and climate projections). In all cases, errors in the upper tail remain below 8%, indicating that the pseudo-generated scenarios accurately reproduce extreme NH magnitudes.

Also, Table III lists the RMSE of the empirical correlograms that have been generating, providing a lumped quantity of discrepancies in spatial dependence between real and pseudo-generated fields. In all cases, this is very low.

Table III. Validation of pseudo-generated stochastic fields against observed extreme-event data

Case	RMSE (99th percentile)	RMSE (of correlogram)
Historical data (1970 - 2005)	0.077	0.202
RCP 4.5 Near-term (2006-2040)	0.064	0.195
RCP 4.5 Mid-century (2041-2070)	0.064	0.185
RCP 4.5 Late-century (2071-2100)	0.068	0.170
RCP 8.5 Near-term (2006-2040)	0.069	0.185
RCP 8.5 Mid-century (2041-2070)	0.060	0.172
RCP 8.5 Late-century (2071-2100)	0.068	0.174

With respect to (*ii*), Figure 13 compares the empirical correlograms, i.e., mean Pearson correlation as a function of inter-site distance, for real and pseudo-generated fields for the historical dataset (Appendix C reports the comparison between generated fields real and pseudo, for all RCPs and time windows). The comparison shows that the pseudo-generated fields reproduce the observed decay of spatial correlation with distance, with negligible discrepancies attributable to dimensionality reduction.

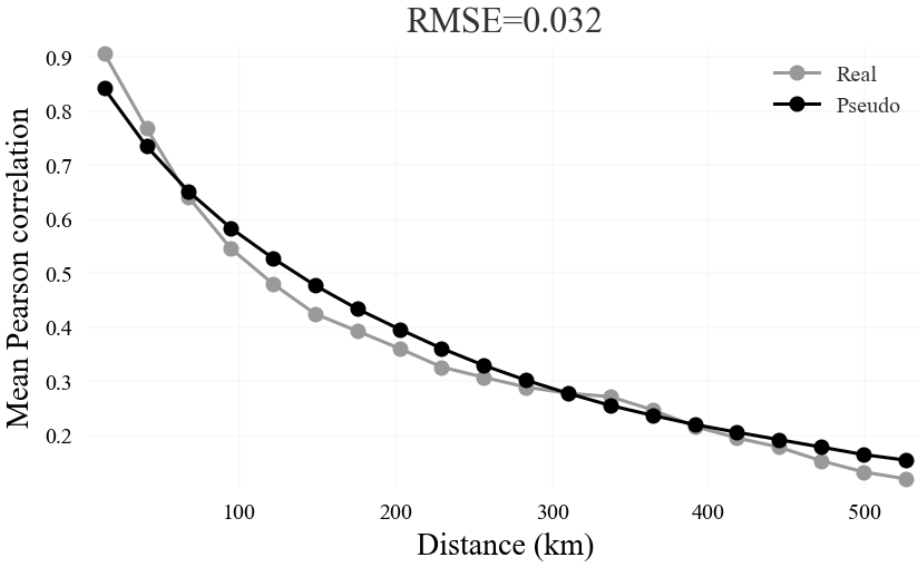

Figure 13. Empirical correlogram of NH fields: real vs pseudo (historical period)

3.3 Multi-state DIIM of the interdependent PN-WN

The stochastic wind-gust scenarios S generated in Section 3.2 are used for the inoperability assessment of the SoS.

Element-level damage in the PN is quantified using a lognormal fragility model that links the 3-second maximum gust velocity at 10 m height to the probability of transmission line failure, coherently with [5] and [72]:

$$\mathbb{P}\left(x^{PN}_{e^{(PN,PN)}_{op},1}\middle|h^{s}_{e^{(PN,PN)}_{op}}\right)=\Phi\left(\frac{ln\left(h^{s}_{e^{(PN,PN)}_{op}}-3.498\right)}{0.056}\right) \quad (20)$$

To ensure consistency of the DIIM here used with that presented in [39], $\bar{\bar{K}}=diag(k_{PN},k_{WN})$ of the DIIM (Equation (12)) is set with $k_{PN}=0.22\ day^{-1}$ and $k_{WN}=0.33\ day^{-1}$, corresponding to characteristic restoration times of 14 and 21 days, respectively. The inoperability space of each CI is discretized into the interval sets:

$$\begin{aligned} r^{PN}&=\{[0],(0,0.3],(0.3,0.5],(0.5,0.7],(0.7,1]\}\\ r^{WN}&=\{[0],(0,0.2],(0.2,0.6],(0.6,0.8],(0.8,1]\}\end{aligned} \quad (21)$$

Following the procedure described in Section 3.2, CI inoperability values obtained across the scenario ensemble are used to empirically estimate the interdependency matrix $\bar{\bar{A}}(t)$ using the interval discretization in Equation (21). For each dependency (PN→WN and WN→PN), an empirical conditional matrix is first estimated from the ensemble scenario outcomes, and interval-specific coefficients are computed using Equations (16) and (17). Because the WN is not directly wind-exposed, the WN→PN dependency ($a_{PN,WN}(r_w^{WN})$) is inferred from stochastically generated WN outages exogenous to wind, whereas the PN→WN dependency ($a_{WN,PN}(r_w^{PN})$) is inferred from wind-induced PN degradation patterns. These conditional matrices define interval-dependent interdependency coefficients, which are subsequently mapped to the time-dependent interdependency matrix $\bar{\bar{A}}(t)$ according to the evolving inoperability state of the CIs. The resulting conditional matrices and extracted coefficients from the historical dataset are shown in Figure 14 and are consistent with the interdependency layout described in Section 3.1.

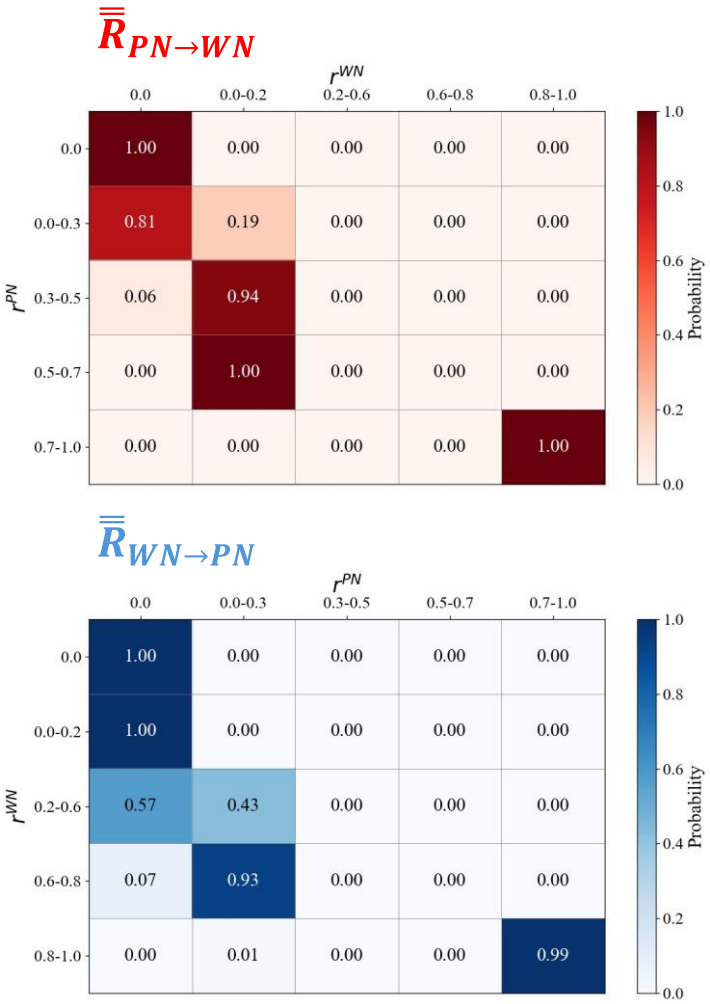

r^{PN}	$a_{WN,PN}[r_w^{PN}]$
[0]	0
(0, 0.3]	0.04
(0.3, 0.5]	0.19
(0.5, 0.7]	0.20
(0.7, 1]	1

r^{WN}	$a_{PN,WN}[r_w^{WN}]$
[0]	0
(0, 0.2]	0
(0.2, 0.6]	0.09
(0.6, 0.8]	0.19
(0.8, 1]	0.99

Figure 14. Conditional probability matrices and interdependency coefficients for PN→WN and WN→PN

The same procedure is applied for each future time window using the climate projections. Table IV summarizes the resulting coefficients. The upper tail ($q_{PN} \geq 0.5$) shows no appreciable change, consistent with saturation: when the PN is highly inoperable, propagation to the WN approaches a structural ceiling largely independent in the scenario. In contrast, most differences occur at intermediate PN inoperability levels PN ($0 < q_{PN} < 0.5$). Under RCP 4.5, the coefficient increases gradually from the near- to far-future periods, whereas under RCP 8.5 it starts higher, exhibits minor fluctuations and reaches its maximum in the late-century slice. Overall, climate forcing does not raise the ceiling of coupling, but it increases the frequency of intermediate PN disruptions, thereby amplifying interdependency cascading failures across SoS.

Table IV. PN→WN Interdependency coefficient re-estimated for each RCP x period

$a_{WN,PN}[r_w^{PN}]$

	RCP 4.5			RCP 8.5		
r^{PN}	Near	Mid	Late	Near	Mid	Late
[0]	0	0	0	0	0	0
(0, 0.3]	0.038	0.040	0.046	0.042	0.044	0.048
(0.3, 0.5]	0.174	0.184	0.190	0.182	0.188	0.194
(0.5, 0.7]	0.200	0.200	0.200	0.200	0.200	0.200
(0.7, 1]	1	1	1	1	1	1

4. Results

Figure 15 shows the temporal evolution of the inoperability of the PN and WN under the historical climate conditions ($\mathcal{T}$ =[1 Jan 1970, 31 Dec 2005]) vs the climate projections RCP 4.5 and RCP 8.5 for near-, mid- and late-century time windows. All DIIMs are initialized, without any loss of generality, with an initial loss of PN capacity temporarily equal to 45% unavailable. Because the WN depends on the PN through the interdependency coefficient $a_{PN,WN}[r_w^{WN}]$, the WN is immediately affected and, then, both networks interact dynamically. It can be seen that the PN inoperability curves are identical for all climate scenarios, since the same interdependency coefficient of WN→PN, recovery rate and initial perturbation are used. In contrast, the WN inoperability curves are different among scenarios, meaning that WN is sensitive to climate-induced variations in the PN→WN dependency. As a result:

- For all time windows, inoperability decreases exponentially over time, confirming the effect of recovery dynamics in the SoS response.
- Under historical climate conditions, both CIs exhibit a rapid decline in inoperability, with the PN returning close to full operability within a few days and the WN following a slightly slower decay due to its dependence on PN recovery. When RCP-specific interdependency coefficients are applied, the WN inoperability curves exhibit only minor deviations from the historical curve. Near-term scenarios show slightly lower inoperability due to weaker effective PN→WN coupling driven by a higher prevalence of moderate, spatially fragmented events, whereas late-century projections (especially under RCP 8.5) result in slightly higher residual inoperability, reflecting stronger coupling associated with more frequent intermediate-to-high disruption events.

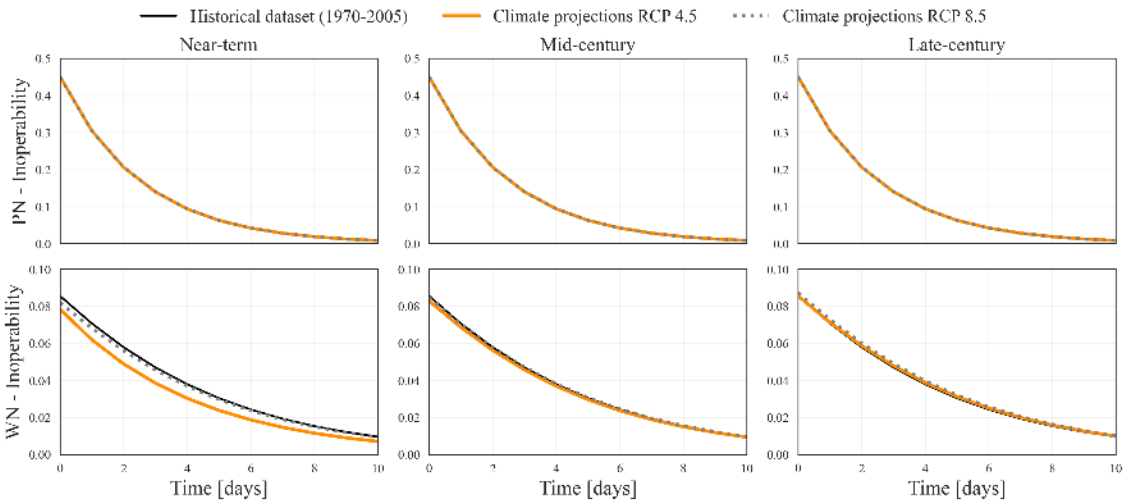

Figure 15. Inoperability of PN and WN under historical and climate scenarios

For an in-depth analysis of the differences between the inoperability curves of WN and to isolate the effect of climate-dependent interdependencies on the WN, for each scenario $rcp \in \{RCP\ 4.5 - near, RCP\ 4.5 - mid, \ldots, RCP\ 8.5 - late\}$, we calculate the WN cumulative inoperability (AUC_{WN}^{rcp}):

$$AUC_{WN}^{rcp} = \int_0^T q_{WN}^{rcp}(t)\, dt \tag{22}$$

and compare it against the AUC_{WN}^{hist} that uses the historical data, as follows:

$$\Delta AUC_{WN}^{rcp} = AUC_{WN}^{rcp} - AUC_{WN}^{hist} \tag{23}$$

ΔAUC_{WN}^{rcp} captures the net effect of climate-conditioned coupling on the total WN inoperability accumulated over the recovery period. Negative values indicate a reduction in cumulative inoperability relative to historical conditions, whereas positive values indicate an increase.

Figure 16 summarizes the resulting ΔAUC_{WN}^{rcp} across RCPs. Under RCP 4.5, the near-term and mid-century horizons exhibit negative values, indicating a lower cumulative WN inoperability than in the historical case, whereas the late-century horizon shows a small positive deviation. Under RCP 8.5, near-term conditions remain slightly negative, the mid-century response is close to neutral, and the late-century displays the largest positive $\Delta AUC_{WN}^{RCP\ 8.5-Late}$, reflecting a higher total inoperability burden.

Importantly, the near-term reduction in cumulative WN inoperability does not imply improved system performance under climate change; it reflects a redistribution of interdependency effects linked to changes in the frequency and spatial organization of moderate events. Climate forcing leaves the recovery shape largely unchanged but increases the cumulative interdependency-driven inoperability in the long term,

especially under stronger forcing.

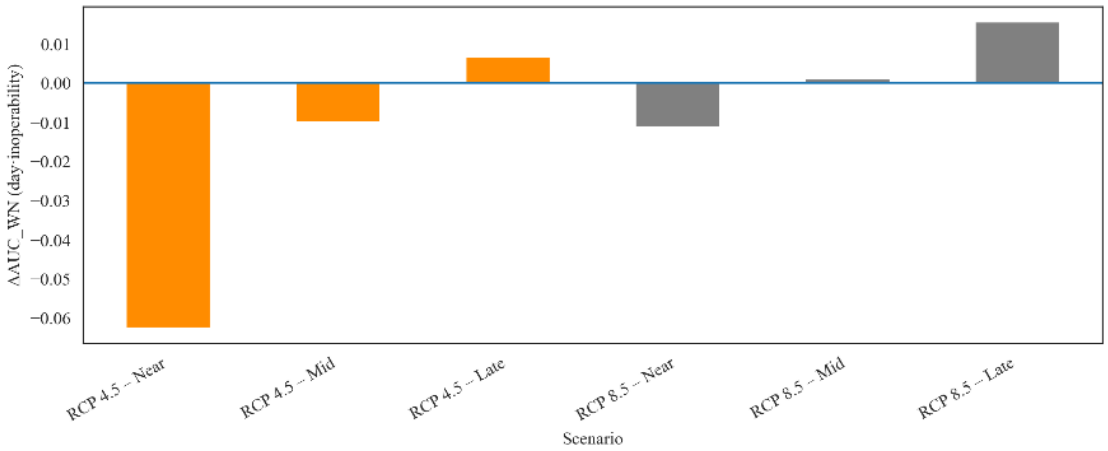

Figure 16. Changes in cumulative WN inoperability relative to the historical baseline

5. Protection of CIs under climate change scenarios

5.1 Protection by prevention

To most effectively prevent CI failures, we identify the transmission lines most critical for the inoperability of the PN exposed to wind gust NH. From this point of view, criticality is not defined solely by local hazard exposure and susceptibility, but also by the role that the lines play with respect to the SoS inoperability resulting from damage cascading through the SoS interdependencies, as described by the SF hazard model coupled with DIIM. Figure 17 and Figure 18 show the top five critical edges identified under historical climate conditions and projected climate conditions, respectively.

Under historical conditions (Figure 17), the most vulnerable transmission lines are located in the northern and central portions of the network, particularly along the Alpine and pre-Alpine corridors. When future climate projections are considered (Figure 18) for both RCP 4.5 (left) and RCP 8.5 (right), two main clusters consistently emerge: one in the northern corridor crossing the Alpine and pre-Alpine regions and another linking central nodes in the southern part of the network. Overall, the results emphasize that climate change exacerbates existing weak points rather than creating new ones.

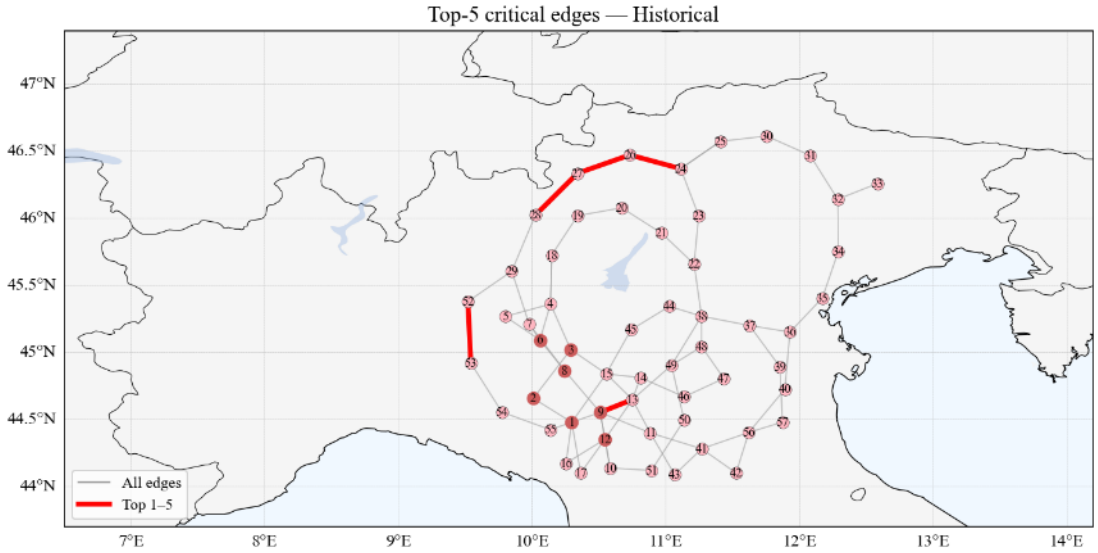

Figure 17. Top five critical edges of the PN under historical wind gust conditions

One can, then, for example, reduce the risk of PN inoperability for near-term climate conditions by preventively retrofitting edges $e_{24,26}^{(PN,PN)}$, $e_{26,27}^{(PN,PN)}$, $e_{27,28}^{(PN,PN)}$ that rank among the most critical edges, where retrofitting is here modeled by assuming full operability of selected transmission lines across all S scenarios. Figure 19 compares the inoperability ratio (r_{PN}) for the baseline case of non-retrofitted edges vs that of the three retrofitted edges, under RCP 4.5 and RCP 8.5. As expected, retrofitting reduces the frequency of moderate-to-severe inoperability states of the CI ($r_{PN} > 0.3$), up to about 30% under RCP 4.5 and up to 25% under RCP 8.5, indicating that targeted retrofitting of a limited number of elements can mitigate propagation-driven operability losses.

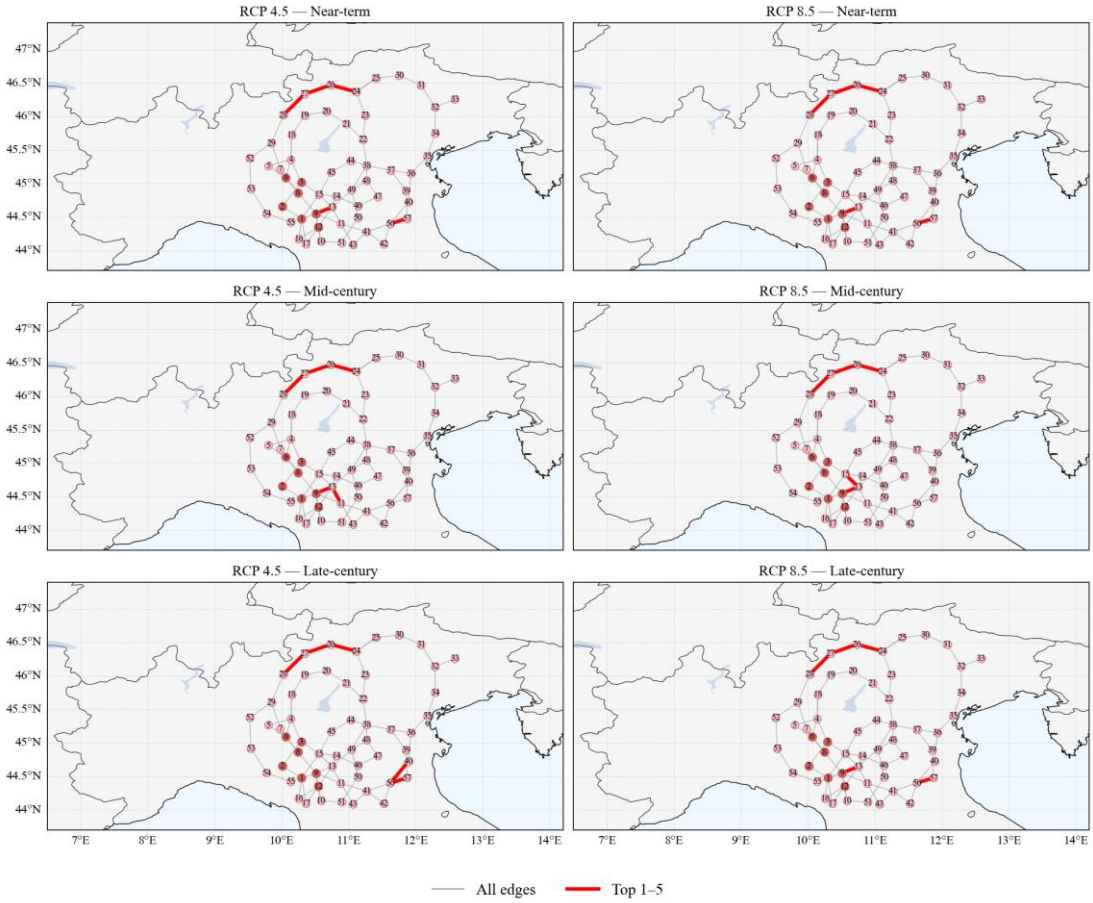

Figure 18. Top five critical edges of the PN under future climate scenarios of wind gust

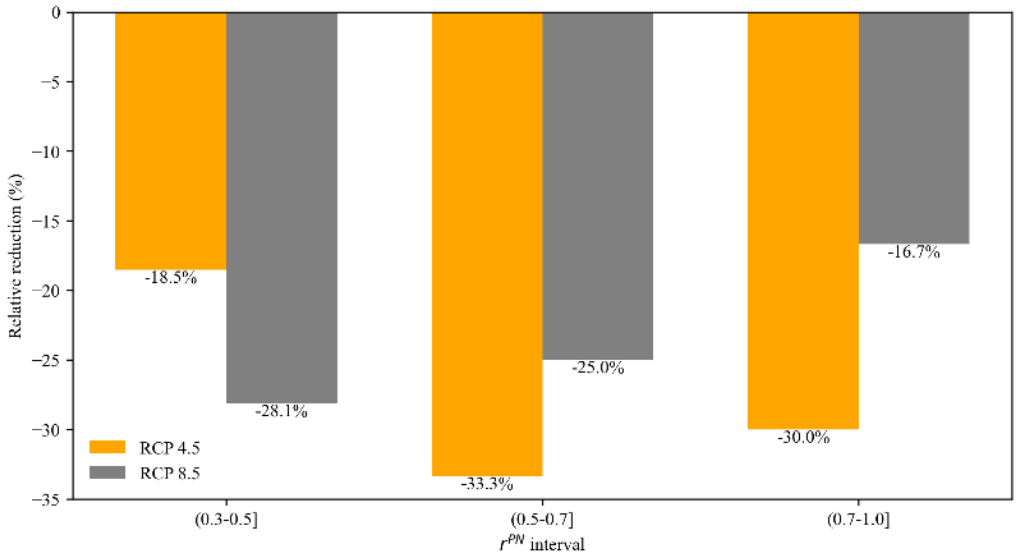

Figure 19. Effect of retrofitting the top three critical edges on near-term power network inoperability

5.2 Protection by mitigation

Mitigation measures can also be undertaken to reduce the consequences of NH scenarios when they occur. Let us, for example, assume that the WN generator can manage to operate for some time but at 50% when power supply from the PN is not available, thanks to backup or local power generation.

Table V summarizes the recalculated PN→WN interdependency coefficient $a_{WN,PN}[r_w^{PN}]$, when we consider the possibility of WN generator operability at 50%, even if PN is not available. Compared with the condition of full dependency (i.e., no alternative power supply, so that the coefficient $a_{WN,PN}[r_w^{PN}]$ is 1 in the PN inoperability interval (0.7, 1], see Table IV), in this case, $a_{WN,PN}(r_w^{PN} = (0.7, 1])$ is kept within [0.58-0.60] for all RCPs and time windows. This reduction indicates that backup generation capability partially alleviates the propagation of severe PN disruptions to the WN, while residual dependency and network-level propagation effects persist. This is also true for moderate PN inoperability intervals $(0.3, 0.5]$, reflecting a general attenuation of dependency strength across different disruption levels.

Table V. PN→WN Interdependency coefficient under mitigation strategy (50% WN generator autonomy)

	$a_{WN,PN}[r_w^{PN}]$					
	RCP 4.5			**RCP 8.5**		
r^{PN}	**Near**	**Mid**	**Late**	**Near**	**Mid**	**Late**
[0]	0	0	0	0	0	0
(0, 0.3]	0.038	0.036	0.044	0.040	0.044	0.040
(0.3, 0.5]	0.162	0.166	0.171	0.167	0.173	0.180
(0.5, 0.7]	0.200	0.200	0.200	0.200	0.200	0.200
(0.7, 1]	0.584	0.600	0.600	0.600	0.600	0.600

The temporal evolution of WN inoperability under the considered mitigation strategy (Figure 20), compared with the original WN inoperability curves (Figure 15), confirms the beneficial effect of reducing dependency on the PN. As shown in Figure 20, low inoperability and fast recovery are observed across all periods and both RCP scenarios. The improvement is more evident under mid-century of RCP 4.5 and late century of RCP 8.5, where higher stress of the PN amplifies the positive effect of partial power generation autonomy by the WN generator. Overall, the mitigated curves show a consistent attenuation of the cascading effects, indicating that even partial reduction of interdependency strengthens the operability of the SoS under future climate conditions.

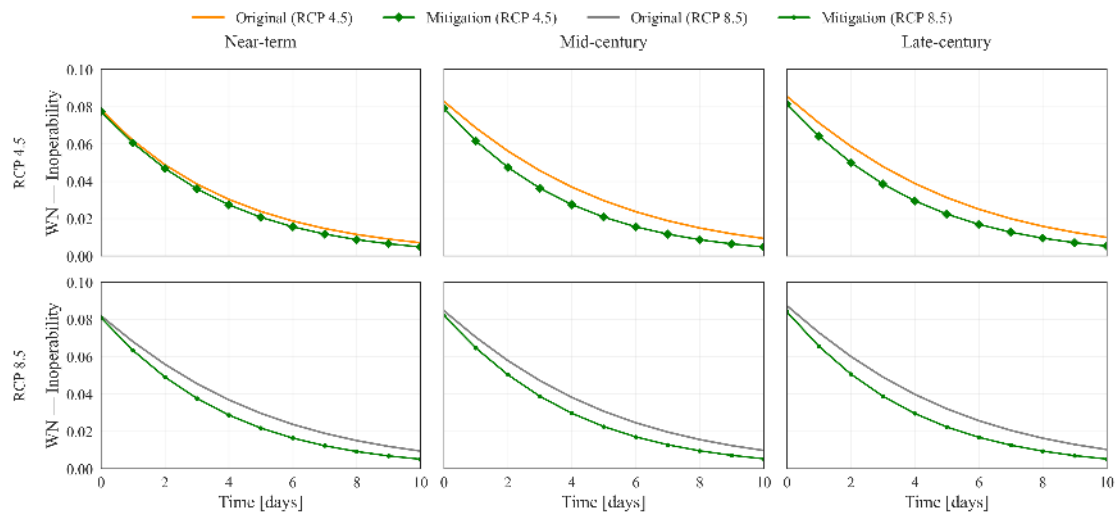

Figure 20. WN inoperability with and without mitigation across RCP 4.5 and RCP 8.5 scenarios

6. Conclusions

This work presents a climate change-informed modeling framework for the inoperability assessment of interdependent critical infrastructures exposed to NHs. The framework integrates: (*i*) stochastic hazard scenarios generated from historical data and climate projections, accounting for NH behavior and spatial dependence; (*ii*) empirical estimation of interdependency coefficients from hazard-induced inoperability realizations; and (*iii*) a multi-state DIIM to propagate cascading effects across a SoS representation of interdependent infrastructures.

The framework is worked out on a case study of interdependent power and water networks in Northern Italy subjected to wind-gust extremes, considering both historical conditions and future climate scenarios (RCP 4.5 and RCP 8.5). A dedicated validation of the SF generation stage demonstrates that the pseudo-generated NH scenarios accurately reproduce both the upper-tail magnitudes and the spatial dependence structure of the original data. Relative errors at the 99th percentile remain below 8% across all cases, whereas empirical correlogram comparisons show limited and scenario-independent discrepancies attributable to dimensionality reduction. This validation supports the suitability of the generated scenarios for downstream cascading failure analyses.

Results from the coupled SF–DIIM framework highlight that climate change primarily affects systemic response through modifications in the frequency and spatial disruption patterns, rather than through large changes in typical hazard intensities. Prevention analysis identifies transmission corridors that consistently emerge as critical across historical and future scenarios, and mitigation experiments illustrate how partial decoupling between CIs can effectively attenuate cascading effects. These outcomes provide actionable insights for prioritizing preventive retrofitting and designing targeted

mitigation strategies under evolving climate conditions.

Although the case study focuses on wind-gust hazards in Northern Italy, the framework is hazard-agnostic by design. The SF generation only requires spatially distributed hazard data, whereas the interdependency estimation and DIIM propagation rely on generic network representations and fragility relationships. As such, the approach can be transferred to other hazard types (e.g., floods, heatwaves, seismic events) and other interdependent infrastructure pairs, using region-specific hazard datasets and component vulnerability models.

Future research will extend the framework in several directions. Uncertainty propagation across hazard modeling and interdependency estimation will be addressed to quantify confidence bounds on systemic inoperability. The current spatial formulation will be extended to spatio-temporal stochastic fields to represent event persistence and evolving dependence under climate change. In addition, multi-hazard and compound events will be considered, and recovery dynamics and resource constraints will be integrated and coupled with optimization or sequential decision-making modules to support cost-effective prevention and mitigation under climate uncertainty.

Acknowledgements

This work was supported by the Italian National Recovery and Resilience programme (PNRR -Piano Nazionale di Ripresa e Resilienza). The authors acknowledge Emmanouil Varouchakis, Professor at the Technical University of Crete, for insightful discussions on variogram modeling and spatial correlation analysis that emerged in the context of the course *Modern Geostatistics for Groundwater Bodies Characterization*, held at Politecnico di Milano, and that supported the development of the stochastic field methodology adopted in this study.

References

[1] Di Pietro, A., Tofani, A., Fuggini, C., Solari, C., & Oliva, G. (2025). An impact risk assessment methodology for the evaluation of the economic, social and operational resilience of critical infrastructures. *International Journal of Disaster Risk Reduction*, *132*, 105965. https://doi.org/10.1016/j.ijdrr.2025.105965

[2] Wang, Y., Zio, E., Wei, X., Zhang, D., & Wu, B. (2018). A resilience perspective on water transport systems: The case of Eastern Star. *International Journal of Disaster Risk Reduction*, *33*, 343-354. https://doi.org/10.1016/j.ijdrr.2018.10.019

[3] Costabile, P., Lombardo, M., Costanzo, C., Tsoukalas, I., & Bellos, V. (2026). A stochastic rain-on-grid framework for handling spatio-temporal rainfall uncertainty in impact-based flood nowcasting. *International Journal of Disaster Risk Reduction*, *134*,

105998. https://doi.org/10.1016/j.ijdrr.2026.105998

[4] Rafi, S., Santos, J., Meng, S., & Mozumder, P. (2025). Extreme Weather Events and Critical Infrastructure Resilience: Lessons from Hurricane Irma in Florida. *Reliability Engineering & System Safety*, 265, 111471. https://doi.org/10.1016/j.ress.2025.111471

[5] Clavijo-Mesa, M.V., Di Maio, F., & Zio, E. (2025). 'Unpublished' A modeling framework for the inoperability assessment of interdependent critical infrastructures exposed to spatially distributed natural hazard. Submitted to *Reliability Engineering & System Safety*.

[6] Summers, J. K., Lamper, A., McMillion, C., & Harwell, L. C. (2022). Observed Changes in the Frequency, Intensity, and Spatial Patterns of Nine Natural Hazards in the United States from 2000 to 2019. *Sustainability*, *14*(7), 4158. https://doi.org/10.3390/su14074158

[7] Wu, C., Zhou, L., Zhang, L., Jin, J., & Zhou, Y. (2019). Precondition cloud algorithm and Copula coupling model-based approach for drought hazard comprehensive assessment. *International Journal of Disaster Risk Reduction*, *38*, 101220. https://doi.org/10.1016/j.ijdrr.2019.101220

[8] Neumann, J. E., Chinowsky, P., Helman, J., Black, M., Fant, C., Strzepek, K., & Martinich, J. (2021). Climate effects on US infrastructure: the economics of adaptation for rail, roads, and coastal development. *Climatic Change*, *167*(3-4). https://doi.org/10.1007/s10584-021-03179-w

[9] Feng, D., Ding, J., Xie, S., Li, Y., Akiyama, M., Lu, Y., Beer, M., & Li, J. (2024). Climate Change Impacts on the Risk Assessment of Concrete Civil Infrastructures. *ASCE OPEN Multidisciplinary Journal of Civil Engineering*, *2*(1). https://doi.org/10.1061/aomjah.aoeng-0026

[10] Rädler, A. T. (2022). Invited perspectives: how does climate change affect the risk of natural hazards? Challenges and step changes from the reinsurance perspective. *Natural Hazards and Earth System Sciences*, *22*(2), 659-664. https://doi.org/10.5194/nhess-22-659-2022

[11] Forzieri, G., Bianchi, A., Silva, F. B. E., Herrera, M. A. M., Leblois, A., Lavalle, C., Aerts, J. C., & Feyen, L. (2017). Escalating impacts of climate extremes on critical infrastructures in Europe. *Global Environmental Change*, *48*, 97-107. https://doi.org/10.1016/j.gloenvcha.2017.11.007

[12] Cremen, G., Galasso, C., & McCloskey, J. (2021). Modelling and quantifying tomorrow's risks from natural hazards. *The Science of The Total Environment*, *817*, 152552. https://doi.org/10.1016/j.scitotenv.2021.152552

[13] Jamous, M., Marsooli, R., & Miller, J. K. (2023). Physics-based modeling of climate change impact on hurricane-induced coastal erosion hazards. *Npj Climate and Atmospheric Science*, *6*(1). https://doi.org/10.1038/s41612-023-00416-0

[14] Faranda, D., Messori, G., Alberti, T., Alvarez-Castro, C., Caby, T., Cavicchia, L., Coppola, E., Donner, R. V., Dubrulle, B., Galfi, V. M., Holmberg, E., Lembo, V., Noyelle, R., Yiou, P., Spagnolo, B., Valenti, D., Vaienti, S., & Wormell, C. (2024). Statistical physics and dynamical systems perspectives on geophysical extreme events. *Physical Review. E*, *110*(4). https://doi.org/10.1103/physreve.110.041001

[15] Alfieri, L., Burek, P., Feyen, L., & Forzieri, G. (2015). Global warming increases the frequency of river floods in Europe. *Hydrology and Earth System Sciences*, *19*(5), 2247-2260. https://doi.org/10.5194/hess-19-2247-2015

[16] Pavesi, L., Volpi, E., & Fiori, A. (2024). Flood risk assessment through large-scale modeling under uncertainty. *Natural Hazards and Earth System Sciences*, 24(12), 4507-4522. https://doi.org/10.5194/nhess-24-4507-2024

[17] Alipour, S. M., Engeland, K., & Leal, J. (2023). Uncertainty analysis of 100-year flood maps under climate change scenarios. *Journal of Hydrology*, *628*, 130502. https://doi.org/10.1016/j.jhydrol.2023.130502

[18] Van Vuuren, D. P., Edmonds, J., Kainuma, M., Riahi, K., Thomson, A., Hibbard, K., Hurtt, G. C., Kram, T., Krey, V., Lamarque, J., Masui, T., Meinshausen, M., Nakicenovic, N., Smith, S. J., & Rose, S. K. (2011). The representative concentration pathways: an overview. *Climatic Change*, *109*(1–2), 5–31. https://doi.org/10.1007/s10584-011-0148-z

[19] Chen, J., Sayama, T., Yamada, M., & Sugawara, Y. (2025). Reducing the computational cost of process-based flood frequency estimation by extracting precipitation events from large-ensemble climate dataset. *Journal of Hydrology*, 132946. https://doi.org/10.1016/j.jhydrol.2025.132946

[20] Katz, R. W. (2010). Statistics of extremes in climate change. *Climatic Change*, 100(1), 71-76. https://doi.org/10.1007/s10584-010-9834-5

[21] Boulaguiem, Y., Zscheischler, J., Vignotto, E., Karin, V. D. W., & Engelke, S. (2021). Modelling and simulating spatial extremes by combining extreme value theory with generative adversarial networks. arXiv (Cornell University). https://doi.org/10.48550/arxiv.2111.00267

[22] Panagoulia, D., Economou, P., & Caroni, C. (2013). Stationary and nonstationary generalized extreme value modelling of extreme precipitation over a mountainous area under climate change. *Environmetrics*, *25*(1), 29-43. https://doi.org/10.1002/env.2252

[23] Jorgensen, S. K., & Nielsen-Gammon, J. W. (2024). Nonstationarity in Extreme Precipitation Return Values Along the United States Gulf and Southeastern Coasts. *Journal of Hydrometeorology*, *25*(5), 771-788. https://doi.org/10.1175/jhm-d-22-0157.1

[24] Westra, S., Fowler, H. J., Evans, J. P., Alexander, L. V., Berg, P., Johnson, F., Kendon, E. J., Lenderink, G., & Roberts, N. M. (2014). Future changes to the intensity and frequency of short-duration extreme rainfall. *Reviews of Geophysics*, *52*(3), 522-555. https://doi.org/10.1002/2014rg000464

[25] Villarini, G., Smith, J. A., Serinaldi, F., Bales, J., Bates, P. D., & Krajewski, W. F. (2009). Flood frequency analysis for nonstationary annual peak records in an urban drainage basin. *Advances in Water Resources*, *32*(8), 1255-1266. https://doi.org/10.1016/j.advwatres.2009.05.003

[26] Earl, N., Dorling, S., Hewston, R., & Von Glasow, R. (2012). 1980–2010 Variability in U.K. Surface Wind Climate. *Journal of Climate*, *26*(4), 1172-1191. https://doi.org/10.1175/jcli-d-12-00026.1

[27] Asaridis, P., Molinari, D., Di Maio, F., Ballio, F., & Zio, E. (2025). A probabilistic modeling and simulation framework for power grid flood risk assessment. *International Journal of Disaster Risk Reduction*, *120*, 105353. https://doi.org/10.1016/j.ijdrr.2025.105353

[28] MacDonald, R., Lee, B. S., Foley, J., & Lee, J. (2025). A Dimension-Reduced Multivariate Spatial Model for Extreme Events: Balancing Flexibility and Scalability. *arXiv (Cornell University)*. https://doi.org/10.48550/arxiv.2501.13070

[29] Brunner, M. I., Furrer, R., & Favre, A. (2019). Modeling the spatial dependence of floods using the Fisher copula. *Hydrology and Earth System Sciences*, 23(1), 107-124. https://doi.org/10.5194/hess-23-107-2019

[30] Khajehali, M., Safavi, H. R., Nikoo, M. R., Najafi, M. R., & Alizadeh-Sh, R. (2025). A copula-based multivariate flood frequency analysis under climate change effects. *Scientific Reports*, *15*(1). https://doi.org/10.1038/s41598-024-84543-5

[31] Fan, Y. R., Yu, L., Shi, X., & Duan, Q. Y. (2021). Tracing Uncertainty Contributors in the Multi-Hazard Risk Analysis for Compound Extremes. *Earth's Future*, *9*(12). https://doi.org/10.1029/2021ef002280

[32] Georgiadis, D. G., & Samuelides, M. S. (2020). Stochastic geometric imperfections of plate elements and their impact on the probabilistic ultimate strength assessment of plates and hull-girders. *Marine Structures*, 76, 102920. https://doi.org/10.1016/j.marstruc.2020.102920

[33] Song, D., Li, Z., Wang, L., Jin, F., Huang, C., Xia, E., Rizk-Allah, R. M., Yang, J., Su, M., & Joo, Y. H. (2022). Energy capture efficiency enhancement of wind turbines via stochastic model predictive yaw control based on intelligent scenarios generation. *Applied Energy*, 312, 118773. https://doi.org/10.1016/j.apenergy.2022.118773

[34] Oh, K., & Nam, W. (2021). A fast Monte-Carlo method to predict failure probability of offshore wind turbine caused by stochastic variations in soil. *Ocean Engineering*, 223, 108635. https://doi.org/10.1016/j.oceaneng.2021.108635

[35] Gaona, M. F. R., Michaelides, K., & Singer, M. B. (2024). STORM v.2: A simple, stochastic rainfall model for exploring the impacts of climate and climate change at and near the land surface in gauged watersheds. *Geoscientific Model Development*, *17*(13), 5387-5412. https://doi.org/10.5194/gmd-17-5387-2024

[36] Panunzio, A. M., Cottereau, R., & Puel, G. (2018). Large scale random fields generation using localized Karhunen–Loève expansion. *Advanced Modeling and Simulation in Engineering Sciences*, 5(1). https://doi.org/10.1186/s40323-018-0114-7

[37] Villa, D. L., Schostek, T., Govertsen, K., & Macmillan, M. (2023). A stochastic model of future extreme temperature events for infrastructure analysis. *Environmental Modelling & Software*, *163*, 105663. https://doi.org/10.1016/j.envsoft.2023.105663

[38] Zeng, D., Zhang, H., Li, Q., & Ellingwood, B. R. (2021). Tropical cyclone damage assessment of distributed infrastructure systems under spatially correlated wind speeds. *Structural Safety*, *91*, 102080. https://doi.org/10.1016/j.strusafe.2021.102080

[39] Mesa, M. V. C., Di Maio, F., & Zio, E. (2025). Dynamic inoperability Input-Output modeling of a system of systems made of Multi-State interdependent critical infrastructures. *Reliability Engineering & System Safety*, 111303. https://doi.org/10.1016/j.ress.2025.111303

[40] Copernicus Climate Change Service. ERA5 post-processed daily-statistics on single levels from 1940 to present. 2024. https://doi.org/10.24381/cds.4991cf48

[41] NASA. NASA World Weather 2025. https://worldwind.arc.nasa.gov/worldweather/ (accessed May 28, 2025).

[42] EURO-CORDEX. The European Coordinated Regional Climate Downscaling Experiment (EURO-CORDEX) data repository. https://www.euro-cordex.net (accessed June 22, 2025).

[43] Shakou, L. M., Wybo, J., Reniers, G., & Boustras, G. (2019). Developing an innovative framework for enhancing the resilience of critical infrastructure to climate change. *Safety Science*, 118, 364–378. https://doi.org/10.1016/j.ssci.2019.05.019

[44] ItaliaMeteo. Europe Meteosat Infrared Map 2025. https://www.agenziaitaliameteo.it/en/meteorology/observed-data/satellite/europe-meteosat-infrared-map/ (accessed May 28, 2025).

[45] Gurney, K. R., Kılkış, Ş., Seto, K. C., Lwasa, S., Moran, D., Riahi, K., Keller, M., Rayner, P., & Luqman, M. (2022). Greenhouse gas emissions from global cities under SSP/RCP scenarios, 1990 to 2100. *Global Environmental Change*, *73*, 102478. https://doi.org/10.1016/j.gloenvcha.2022.102478

[46] Riahi, K., Rao, S., Krey, V., Cho, C., Chirkov, V., Fischer, G., Kindermann, G., Nakicenovic, N., & Rafaj, P. (2011). RCP 8.5—A scenario of comparatively high greenhouse gas emissions. *Climatic Change*, *109*(1-2), 33-57. https://doi.org/10.1007/s10584-011-0149-y

[47] Copernicus Climate Change Service. ERA5 post-processed daily-statistics on single levels from 1940 to present. 2024. https://doi.org/10.24381/cds.4991cf48

[48] WMO. Guidelines on Analysis of extremes in a changing climate in support of informed decisions for adaptation. Geneva: 2009.

[49] Schwarz G. Estimating the Dimension of a Model. The Annals of Statistics 1978;6. https://doi.org/10.1214/aos/1176344136

[50] Akaike H. A new look at the statistical model identification. *IEEE Transactions on Automatic Control* 1974;19:716–23. https://doi.org/10.1109/TAC.1974.1100705

[51] Massey, F. J. (1951). The Kolmogorov-Smirnov test for goodness of fit. *Journal of the American Statistical Association*, *46*(253), 68. https://doi.org/10.2307/2280095

[52] Anderson, T. W., & Darling, D. A. (1952). Asymptotic theory of certain "Goodness of fit" criteria based on stochastic processes. *The Annals of Mathematical Statistics*, *23*(2), 193–212. https://doi.org/10.1214/aoms/1177729437

[53] Wilk, M. B., & Gnanadesikan, R. (1968). Probability plotting methods for the analysis of data. *Biometrika*, *55*(1), 1. https://doi.org/10.2307/2334448

[54] Cressie, N. a. C. (1993). Statistics for spatial data. In *Wiley series in probability and statistics*. https://doi.org/10.1002/9781119115151

[55] Prasetya, D. A., Nguyen, P. T., Faizullin, R., Iswanto, I., & Armay, E. F. (2020). Resolving the shortest path problem using the haversine algorithm. *Journal of Critical Reviews*, *7*(1), 62–64. https://doi.org/10.22159/jcr.07.01.11

[56] Cressie, N. (1985). Fitting variogram models by weighted least squares. *Mathematical Geology*, *17*(5), 563–586. https://doi.org/10.1007/bf01032109

[57] Porcu, E., Furrer, R., & Nychka, D. (2020). 30 Years of space–time covariance functions. *Wiley Interdisciplinary Reviews Computational Statistics*, *13*(2). https://doi.org/10.1002/wics.1512

[58] Fleermann, M., & Heiny, J. (2022). Large Sample Covariance Matrices of Gaussian Observations with Uniform Correlation Decay. *arXiv (Cornell University)*. https://doi.org/10.48550/arxiv.2203.04057

[59] Dong, J., Cui, W., & Liu, Y. (2025). Covariance Matrix Estimation from Correlated Sub-Gaussian Samples via the Shrinkage Estimator. *IEEE Signal Processing Letters*, 1–5. https://doi.org/10.1109/lsp.2025.3541427

[60] Betz, W., Papaioannou, I., & Straub, D. (2014b). Numerical methods for the discretization of random fields by means of the Karhunen–Loève expansion. *Computer Methods in Applied Mechanics and Engineering*, *271*, 109–129. https://doi.org/10.1016/j.cma.2013.12.010

[61] Daw, R., Simpson, M., Wikle, C. K., Holan, S. H., & Bradley, J. R. (2022). An overview of univariate and multivariate Karhunen Loève expansions in statistics. *Journal of the Indian Society for Probability and Statistics*, *23*(2), 285–326. https://doi.org/10.1007/s41096-022-00122-9

[62] Giannetti, F., Pecchi, M., Travaglini, D., Francini, S., D'Amico, G., Vangi, E., Cocozza, C., & Chirici, G. (2021). Estimating VAIA Windstorm Damaged Forest Area in Italy Using Time Series Sentinel-2 Imagery and Continuous Change Detection Algorithms. *Forests*, *12*(6), 680. https://doi.org/10.3390/f12060680

[63] MATPOWER. Case 57 Power flow data for IEEE 57 bus test case. https://MatpowerOrg/Docs/Ref/Matpower50/Case57Html 2014

[64] Medina-Quesada, Á., Montoya, O. D., & Hernández, J. C. (2022). Derivative-Free Power Flow Solution for Bipolar DC Networks with Multiple Constant Power Terminals. *Sensors*, *22*(8), 2914. https://doi.org/10.3390/s22082914

[65] KNMI – Koninklijk Nederlands Meteorologisch Instituut. Ministerie van Infrastructuur en Waterstaat. Potential wind. (November, 2025). https://www.knmi.nl/kennis-en-datacentrum/project/potential-wind

[66] Kotlarski, S., Keuler, K., Christensen, O. B., Colette, A., Déqué, M., Gobiet, A., Goergen, K., Jacob, D., Lüthi, D., Van Meijgaard, E., Nikulin, G., Schär, C., Teichmann, C., Vautard, R., Warrach-Sagi, K., & Wulfmeyer, V. (2014). Regional climate modeling on European scales: a joint standard evaluation of the EURO-CORDEX RCM ensemble. *Geoscientific Model Development*, *7*(4), 1297-1333. https://doi.org/10.5194/gmd-7-1297-2014

[67] Jacob, D., Petersen, J., Eggert, B., Alias, A., Christensen, O. B., Bouwer, L. M., Braun, A., Colette, A., Déqué, M., Georgievski, G., Georgopoulou, E., Gobiet, A., Menut, L., Nikulin, G., Haensler, A., Hempelmann, N., Jones, C., Keuler, K., Kovats, S., . . . Yiou, P. (2013). EURO-CORDEX: new high-resolution climate change projections for European impact research. *Regional Environmental Change*, *14*(2), 563-578. https://doi.org/10.1007/s10113-013-0499-2

[68] Panteli, M., Pickering, C., Wilkinson, S., Dawson, R., & Mancarella, P. (2016). Power System Resilience to Extreme Weather: Fragility Modeling, Probabilistic Impact Assessment, and Adaptation Measures. *IEEE Transactions on Power Systems*, *32*(5), 3747-3757. https://doi.org/10.1109/tpwrs.2016.2641463

[69] Ma, N., Xu, Z., Wang, Y., Liu, G., Xin, L., Liu, D., Liu, Z., Shi, J., & Chen, C. (2024). Strategies for Improving the Resiliency of Distribution Networks in Electric Power Systems during Typhoon and Water-Logging Disasters. *Energies*, *17*(5), 1165. https://doi.org/10.3390/en17051165

[70] Serrano-Fontova, A., Li, H., Liao, Z., Jamieson, M. R., Serrano, R., Parisio, A., & Panteli, M. (2023). A Comprehensive Review and Comparison of the Fragility Curves Used for Resilience Assessments in Power Systems. *IEEE Access*, *11*, 108050-108067. https://doi.org/10.1109/access.2023.3320579

[71] North, G. R., Bell, T. L., Cahalan, R. F., & Moeng, F. J. (1982). Sampling Errors in the Estimation of Empirical Orthogonal Functions. *Monthly Weather Review*, *110*(7), 699-706. https://doi.org/10.1175/1520-0493(1982)110

[72] Wang, J., Li, H., Fu, X., Dong, Z., & Sun, Z. (2022). Wind fragility assessment and sensitivity analysis for a transmission tower-line system. *Journal of Wind Engineering and Industrial Aerodynamics*, *231*, 105233. https://doi.org/10.1016/j.jweia.2022.105233

Appendix A. PN-WN Interdependency mapping

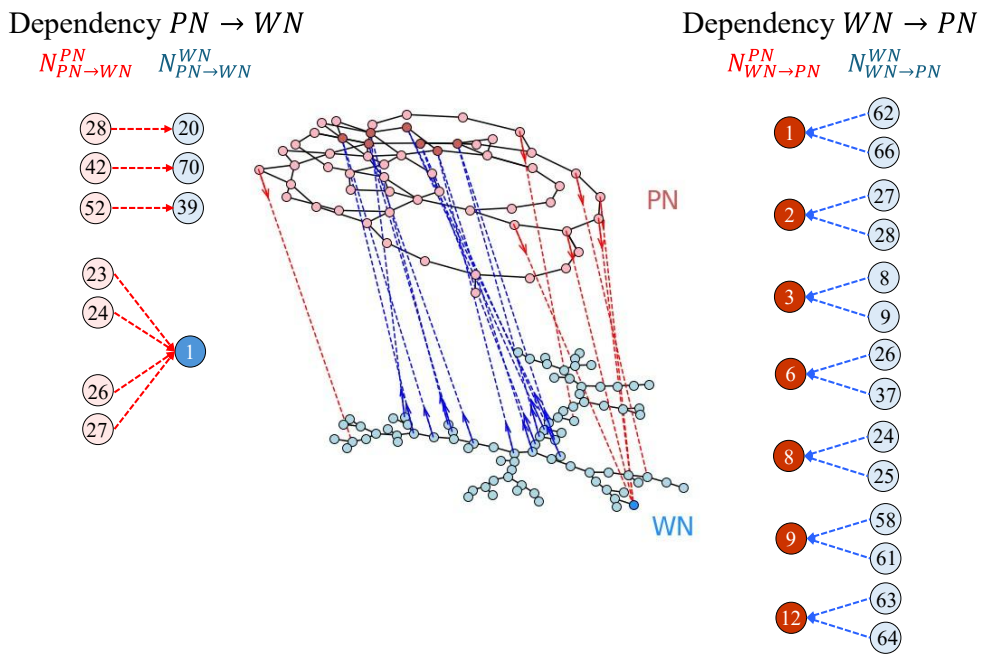

Figure A 1. Interdependency mapping between PN and WN

Appendix B. Spatial distribution of best-fit marginal for RCP 4.5 and RCP 8.5

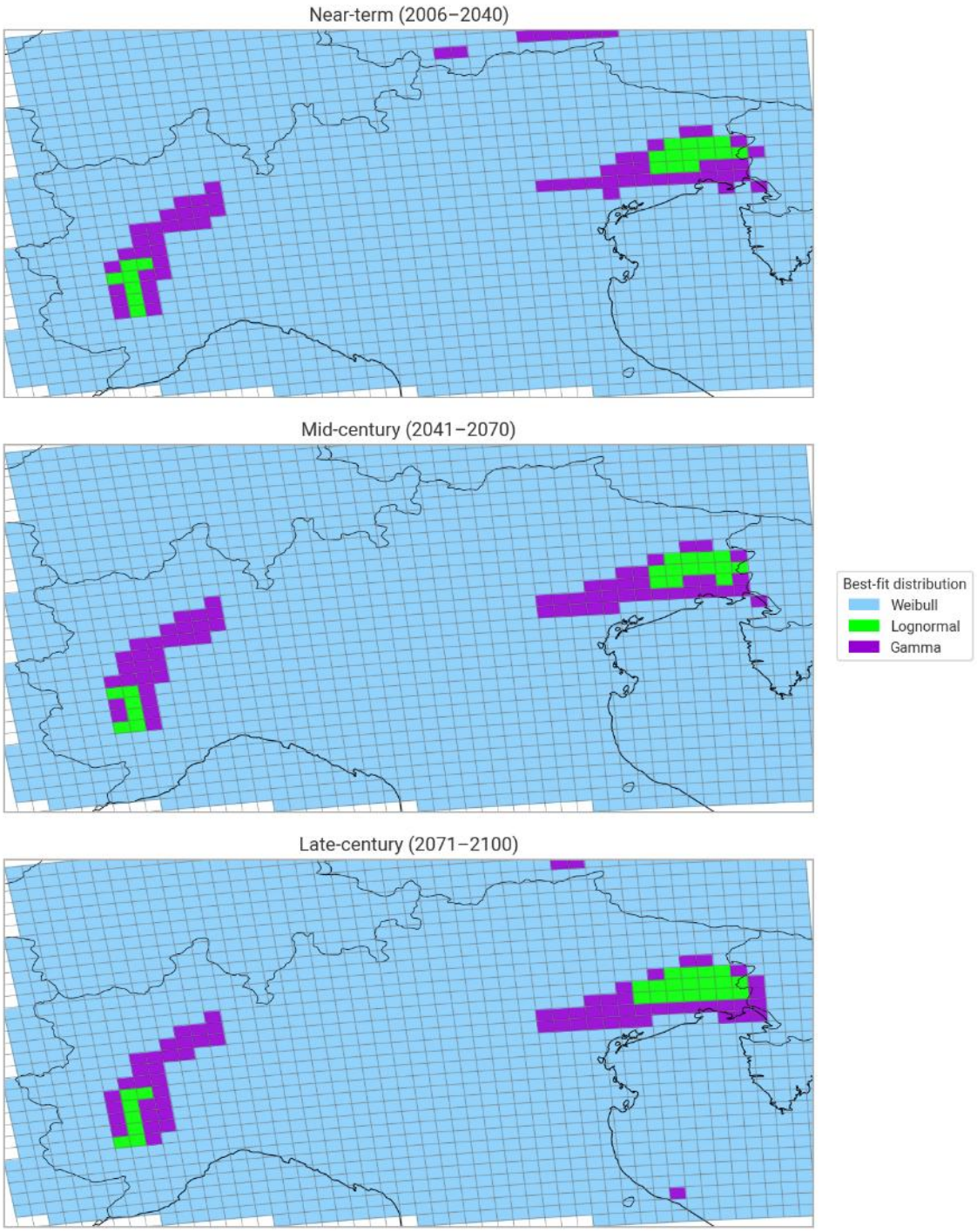

Figure B 1. Spatial distribution of best-fit marginal families for wind-gust data (RCP 4.5)

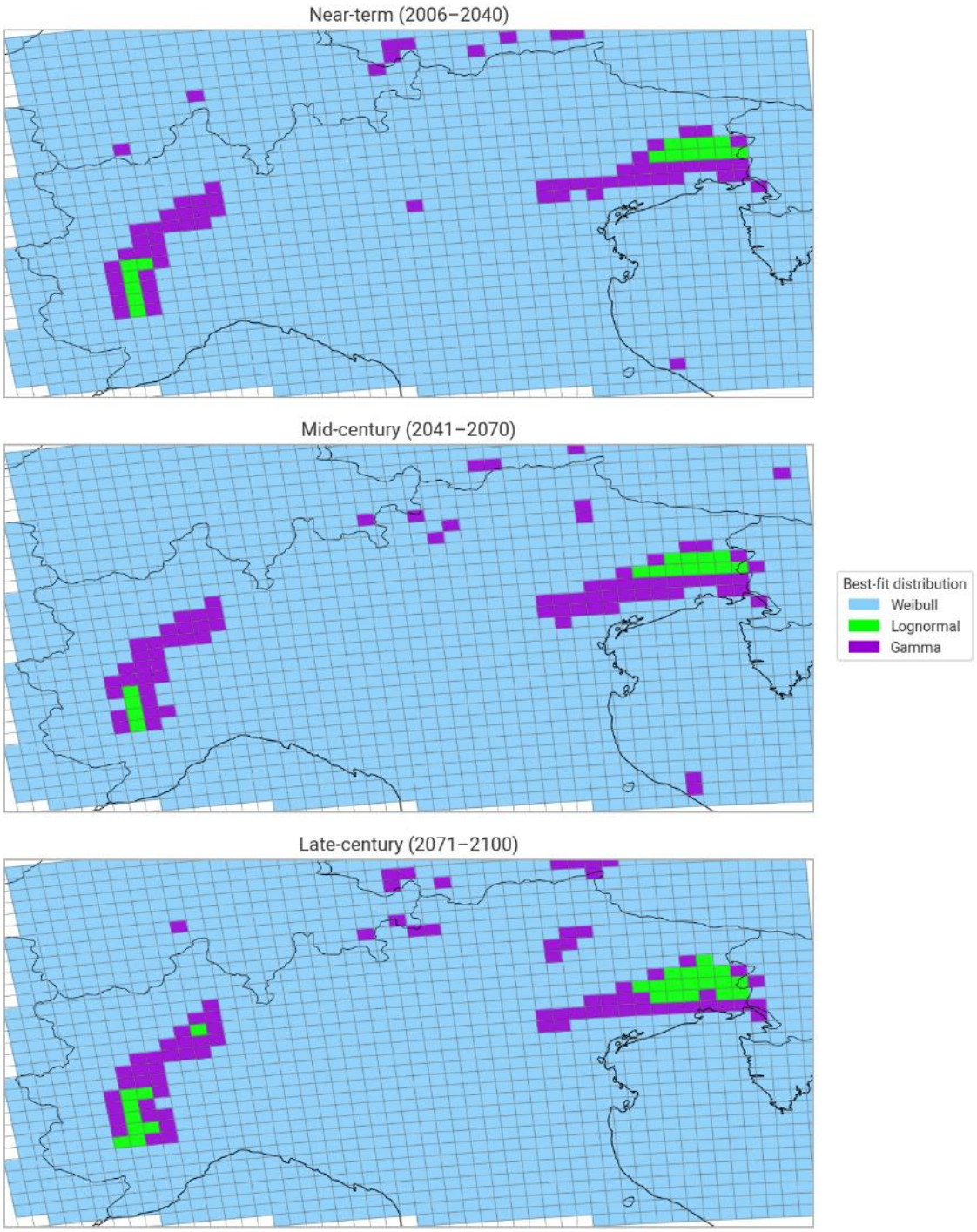

Figure B 2. Spatial distribution of best-fit marginal families for wind-gust data (RCP 8.5)

Appendix C. Spatial-dependence validation of pseudo-generated fields across climate scenarios

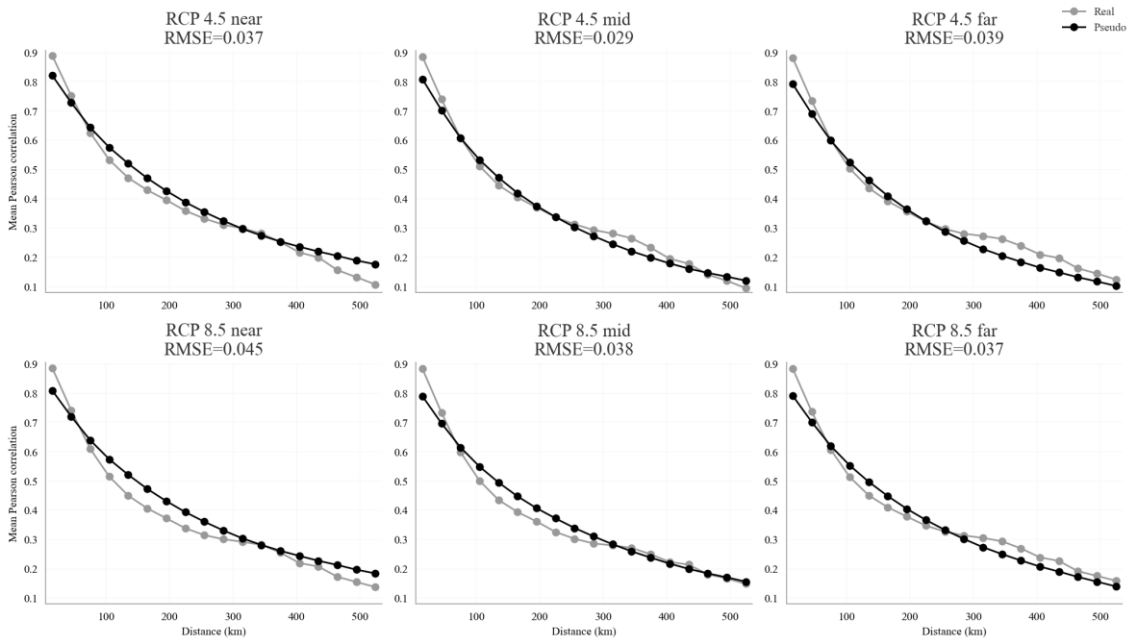

Figure C1. Empirical correlogram comparison between real and pseudo-generated fields across RCPs and time windows